Torque Generation In The Bacterial Flagellar Motor

STUART REID

A thesis submitted in partial fulfillment of
the requirements for the degree of
Doctor of Philosophy at the University of Oxford

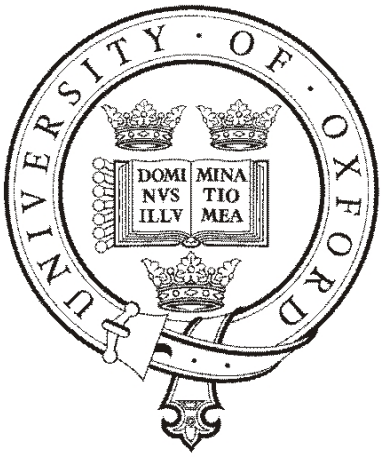

Wadham College
University of Oxford
Michelmas Term 2006

Torque Generation in the Bacterial Flagellar Motor

Stuart Reid, Wadham College.

Thesis submitted for the degree of Doctor of Philosophy
at the University of Oxford, Michelmas Term 2006.

Abstract

The bacterial flagellar motor is a powerful, ion-driven molecular motor. Situated in the cell wall of swimming bacteria such as *E. coli* or *Salmonella*, the motor drives helical flagellar filaments propelling the bacteria through the liquid environments they inhabit. The torque-generating stator units are composed of the proteins MotA and MotB in proton-driven motors and PomA and PomB in sodium-driven motors. Units are anchored to the cell wall and use the ion-motive force across the cell membrane to apply torque to the central rotor.

This thesis demonstrates control of the number of torque generators in a motor by induction from plasmids. The number of units in a full motor is determined and the dependence of motor properties on torque generator number is investigated. An assay is developed in order to study stepping in the rotation of the motor with fluorescent photodamage complications removed.

Acknowledgements

The first thanks should go to my family who have supported me through my rather longer than anticipated university career. Next (chronologically) the Physics tutors at Wadham. Sukumar who almost single handedly taught me the whole of Physics and Graham, who over a glass of whisky at schools dinner, helped me to decide a D.Phil was the way forward. Dave, Maureen and the rest of the staff at the DTC who invented the life sciences interface as I know it. Of course the ever enthusiastic supervisor Richard gets a big mention here.

Everyone in and around the group, labs, DTC, college, sports teams (that includes darts) who have contributed either academically or socially to this body of work (formal research contributions are listed below) are too numerous to list but you know who you are.

Financial Support EPSRC, LSIDTC, Bionanotechnology IRC.

Research contributions Several members of the lab have performed and assisted with experiments included in this thesis. These contributions are listed here and detailed in footnotes where they appear.

Some of the resurrection data and controls were collected by Mark Leake (ML) our postdoc and Richard Berry (RB) my supervisor. Immunoblots were carried out by Jennifer Chandler (JC) in the laboratory of Judy Armitage. JC also assisted with the construction of the MotAB strain. Chimera strain resurrections and steady state induction measurements were carried out by Chien-Jung Lo (CJL) a fellow D. Phil student.

Stuart Reid
Oxford, December 2006

Contents

Chapter 1

Biophysics, motors and motility

1.1 Science between disciplines

Interesting questions in science are often no longer contained within the historical divisions of Physics, Chemistry and Biology but instead lie between these disciplines. Bionanotechnology is a field that has emerged over the last few decades and is an example of this interdisciplinary science, requiring knowledge of areas ranging from materials science to cell biology. There are many challenges in the realm of nanotechnology where behaviour of materials and systems are often vastly different from those on larger length scales. The manipulation of single molecules to perform a specific task or function is

demanding in all but the simplest of systems. Many challenges have already been overcome by nature and the study of these existing systems provides both insight into the natural world and a means to utilise existing technology to help achieve our goals.

Research topics in bionanotechnology not only satisfy scientific curiosity or are "blue sky" type research but also have the potential to deliver benefits in the form of medical and technological advances. Drug discovery is a major potential benefit where, if the interactions between particular molecules and cell receptors is better understood, drugs can be designed to specifically target these sites. These drugs may also need to be delivered to a particular area of the body, for example a tumour, and it is conceivable that biological or biologically inspired motors may provide propulsion for a delivery system.

This thesis will first set the context and motivation for the study of molecular motors, in particular the bacterial flagellar motor (this chapter). Chapter 2 will then give a detailed explanation of the flagellar motor, its structure and function, building on the most recent (2003) literature reviews and incorporating new results, focusing on the area of torque generation. Chapter 3 details the experimental techniques, biochemical, optical and computational, that are used in subsequent chapters. Chapters 4 and 5 describe the main experimental results obtained during this research with insights into the number and arrangement of torque-generating units and their detailed function.

The final chapter draws together these results, highlights the questions that have been answered, remain to be answered and have been raised by this work.

1.2 Molecular machines

The Oxford English Dictionary (Oxford University Press, 2002) defines a molecular machine as either "a complex molecule which carries out a specific physical or chemical task", or "a nanotechnological machine or device." This thesis is concerned with the study of naturally occurring molecular machines that have been refined over millions of years by evolution. These machines are far more advanced than those we can currently construct artificially so a more specific definition of "a macromolecule or macromolecular complex that performs a task or function for a living organism," is appropriate.

Molecular machines are integral parts of living cells and are responsible for many of the characteristics exhibited that allow us to define them as living. Exact definitions of life continue to be hotly debated (the online encyclopedia entry (Wikipedia contributors, 2006) is under constant revision) but examples of molecular machines, and in many cases motors, performing tasks that correspond to some of the more conventional definitions (in italics) can be explored. Linear motors contribute to intracellular *organisation*,

transporting vesicles and macromolecules along cytoskeletal tracks. Numerous pieces of machinery operate on and around DNA, replicating, repairing and translating the genome allowing cells and organisms to *reproduce*, *adapt* and *respond* to a changing environment. A diverse group of molecular machines is the enzymes (a PDB search (Berman et al., 2000) reveals more than 5000 structures) that catalyse biological reactions, *metabolism*, essential for life.

Of all molecular machines, the class of motors stands out as their effects are directly observable on a range of length scales from microscopic cellular transport, for example cytoplasmic streaming, to the muscle movements of macroscopic organisms.

1.3 Molecular motors

Naturally occurring molecular motors are remarkable pieces of engineering. They operate in the inhospitable environment of the nanoscale, where the Reynolds number is low, momentum is negligible and Brownian motion delivers frequent forceful blows from random directions. Despite these challenges, molecular motors are reliable (life depends on it), efficient (some motors operate close to 100 %) and powerful (human muscle for example). Motors can be considered in two classes: the linear motors, stepping along custom built

tracks, and the rotary motors, usually fixed in membranes.

1.3.1 Energy considerations

Biological organisms maintain two main energy sources that are harnessed by molecular motors, a supply of adenosine triphosphate (ATP), occasionally the similar molecule guanine triphosphate (GTP), and the ion-motive force across cell membranes. These two energy sources are well regulated by cells and are also interlinked by multiple pathways, including ATP driven ion pumps and ion driven ATP-synthase.

At room temperature, the thermal energy (k_BT) is approximately 4×10^{-21} J. It is conventional to work in units corresponding to the scales on which these motors operate, forces of pN and distances of nm. The thermal energy is therefore 4 pN·nm or 1 k_BT. Under physiological conditions, an ATP hydrolysis ($ATP \rightarrow ADP + P_i$) releases between 20 and 24 k_BT of which about half is enthalphic, the rest entropic[1]. A monovalent ion transition over a typical cell membrane voltage delivers about 6 k_BT[2].

There are two classes of mechanism that describe how a molecular motor operates, either as a Brownian ratchet or by a powerstroke mechanism.

[1]The energy released is a function of the reactant and product concentrations. The range of values quoted are for a typical cell.

[2]A monovalent ion, 1.6×10^{-19}C through a membrane potential of 150 mV at room temperature.

These can be illustrated by considering the progression of a small particle in one dimension. The Brownian ratchet describes a motor that rectifies large scale random fluctuations by imposing a high energy barrier. In our model the small particle executes a random walk along the motion coordinate. If the particle passes a defined point, for example 100 fluctuations to the right of the starting coordinate, a high potential energy barrier is imposed, effectively infinite, and the motor has taken one "step". This process is then repeated and the motor travels to the right. The powerstroke mechanism is illustrated by the same particle but with a smooth driving potential present. The particle then steadily moves to the right but still experiences Brownian motion superimposed on this movement. The powerstroke mechanism is indistinguishable from a Brownian ratchet that rectifies small scale fluctuations with a low potential barrier which is why the term Brownian ratchet is only applied to rectification of large fluctuations. These two mechanisms represent extremes and in practice most motors will operate as a combination of the two (Oster and Wang, 2003*a*).

Since molecular motors can operate at near equilibrium conditions it is possible to reach very high thermodynamic efficiency. Linear motors such as myosin and kinesin reach up to about 50 % (Howard, 1996; Takagi et al., 2006; Finer et al., 1995) and the F_1 motor of the ATP synthase approaches 100 % (Kinosita et al., 1998).

1.3.2 Linear motors

A common feature of linear motors is that they operate in a preferred direction with head domains binding at specific points along a particular track and tails attached to a cargo. Linear motors exist that operate along DNA or RNA tracks such as polymerases and helicases (artificial motors are also designed that run along custom DNA tracks (Seeman, 2005)) but the best studied and understood motors operate along either microtubules or actin filaments. Most of these motors operate independently in a processive manner (high duty ratio), walking along their tracks and dragging a cargo but one of the more familiar motors, muscle myosin, rows along its actin track in cooperation with numerous identical heads generating the explosive power and large scale movements we see in human muscle on a day to day basis.

Myosin II: a rower

Myosin II is an excellent model system to illustrate how the small scale motion of molecular motors can be scaled up to generate large forces and motions. Also known as conventional myosin or muscle myosin, this is a two headed motor (Liang et al., 1999) with the heads linked by wound alpha helices that serve to connect the molecules together. Each head binds to actin filaments generating a power stroke on hydrolysis of an ATP molecule.

It is tempting to suppose that two heads imply a precessive mechanism (a walker) but this is not the case since each head spends only a small fraction of its time bound to the track (a low duty ratio).

Muscles are arranged with alternating thick and thin filaments. Thick filaments are formed from multiple myosin IIs with the tail chains intertwined forming a many headed structure with each head facing the same direction. The thin filaments are the actin tracks against which the thick filaments slide. The relative motion of thick and thin filaments causes contraction of muscle cells with the combined motion of many cells in parallel and series multiplying force and movement respectively.

The generally accepted model for the acto-myosin system is the swinging lever arm model (Geeves and Holmes, 1999). In the absence of ATP, myosin is bound to actin in a rigor complex. ATP binding at the catalytic site allows the head to release and hydrolysis of ATP causes the lever to extend. The head then binds the actin along from the initial site. The release of the hydrolysis products contracts the arm, the power stroke, returning the myosin to the original state but with thin and thick filaments shifted relative to each other. In vitro assays of single myosin II molecules show step sizes of $\sim$4 nm (Molloy et al., 1995) and forces of $\sim$2 pN consistent with this model. Figure 1.1 shows a ribbon model of a myosin fragment in states before and after the working stroke. The fragment contains the catalytic site and the

actin binding domain and illustrates the extension of the lever arm during the working stroke. Myosin II is just one of 18 classes of myosin well studied by recent single molecule techniques (Ruegg et al., 2002). Other studied myosins classes are myosin I, a singled headed motor (Veigel et al., 1999), myosin IV, that operates in the opposite direction (Lister et al., 2004) and myosin V, a walker.

Kinesin: a walker

The walking linear motors consist of two often identical head groups, each of which is capable of generating the power stroke, linked by tail groups that are responsible for the cargo. The Kinesin superfamily of proteins that operate along microtubules are good examples of this type of motor although Myosin V/actin (Sellers and Veigel, 2006) and Dynein/microtubule (Reck-Peterson et al., 2006) systems also operate in a similar fashion.

Kinesins are found that walk in either direction along microtubules. They are responsible for the transport of organelles and macromolecular complexes, are essential for cell division, participate in the sliding and bundling of microtubules and perform many other functions in a cell. Conventional kinesin travels towards the plus end of the microtubule in a hand over hand fashion (Yildiz et al., 2004). There are several detailed models for the mechanism of kinesin stepping each of which explains the experimental data of forwards and

Figure 1.1: Ribbon representation of the structure of a Myosin II fragment (left) bound to the actin filament (right). The states before (top) and after (bottom) the working stroke are shown illustrating the conformational change that generates relative linear motion. Figure adapted from Geeves and Holmes, 1999.

backwards stepping under various applied load. Models differ as to whether the mechanism is a power stroke and lever arm (Shao and Gao, 2006), a spring-like stretch of the neck (Rosenfeld et al., 2003) or perhaps a combination of these (Carter and Cross, 2005).

Figure 1.2 shows a ribbon model of the two kinesin heads and the kinesin stepping mechanism of a forwards step as proposed by Carter and Cross, 2005. The two-headed kinesin begins with an ADP containing free head and an empty head bound to the track (Figure 1.2 0, parked). ATP binding at the bound head allows release of ADP from the free head when it binds either in front of or behind the bound head depending on the applied load (Figure 1.2 +1, +2, +3). Hydrolysis of the ATP during this step may drive a conformational change necessary to allow binding of the second head. Release of the phosphate from the initially bound head (Figure 1.2 +3) releases this head and the kinesin has completed a step (Figure 1.2 0, parked).

1.3.3 Rotary motors

There are two rotary molecular motor systems (three individual motors) identified and studied to date. They are the F_1F_OATP synthase (consisting of two motors) and the bacterial flagellar motor. Both the flagellar motor and the F_O part of ATP synthase are membrane bound and harness the ion-

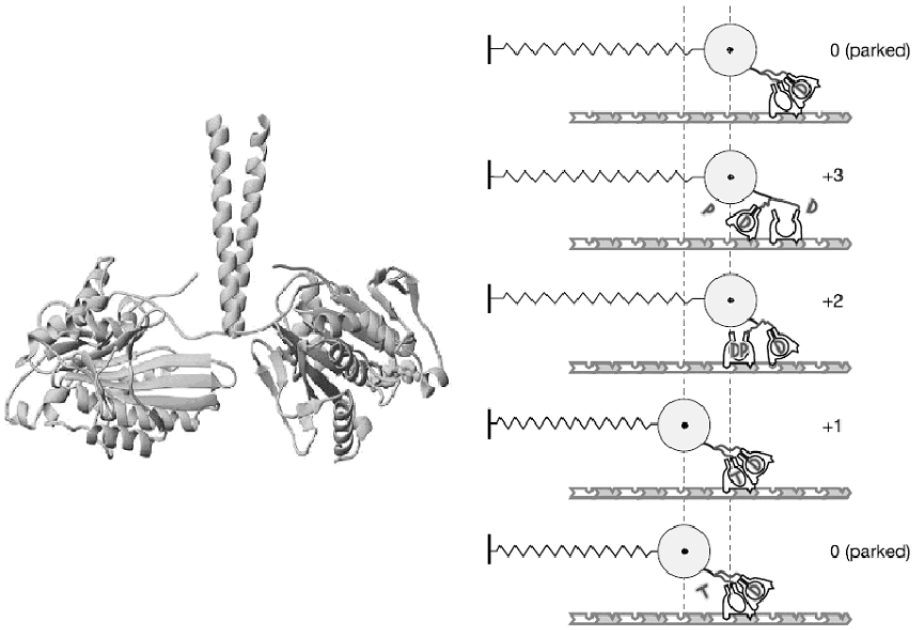

Figure 1.2: A ribbon structure of the kinesin heads (left) and the mechanism of a forwards step under an applied load (right). The structure shows bound ADP at the catalytic site of the right hand head. The structure and mechanism were adapted from Yildiz et al., 2004 and Carter and Cross, 2005 respectively.

motive force across the membrane to generate rotary motion. The F_1 part of ATP synthase is ATP driven. There are other ATPase proteins thought to operate as rotary motors, one group being the helicases, however this has not yet been demonstrated (Oster and Wang, 2003*b*).

F_1F_OATP synthase

ATP synthase maintains a supply of free energy (in the form of ATP) and is found in the membranes of bacteria and energy producing organelles such as mitochondria or chloroplasts. The synthase can be thought of as two separate motors coupled by a common rotor. Under normal conditions F_O harnesses the proton-motive force to generate rotary motion driving the common rotor. The rotor then drives conformational changes in the three fold symmetric F_1 that converts adenosine diphosphate (ADP) to ATP, three molecules per full rotation. The motor is also capable of operating in reverse, consuming ATP to maintain the proton-motive force under starvation conditions (Diez et al., 2004; Itoh et al., 2004). Recent reviews are available (Weber and Senior, 2003; Oster and Wang, 2003*b*). A diagram of the F_1F_OATP synthase in shown in Figure 1.3 with the protein subunits labelled.

The F_O motor is embedded in the membrane and the F_1 motor, which is soluble, exists in the cytoplasm. The two parts of the enzyme are easily separated under mild conditions. The separated motors both retain their activity,

with the F_O remaining in the membrane acting as a passive bi-directional proton filter, and the F_1 acting as an ATPase free in solution. The soluble nature of F_1 makes it more amenable to study, in particular to crystallisation, and is therefore more thoroughly understood than the membrane bound F_O.

The F_1 motor makes three 120 degree steps per rotation, each of which is split into an 80 degree and a 40 degree substep (Shimabukuro et al., 2003). These substeps are identified with ATP binding and hydrolysis product release respectively (Yasuda et al., 2001). Steps are due to a conformational change in the β subunits (Figure 1.3) driven by ATP binding and can be likened to the powerstroke in linear motors, for example Myosin II.

Bacterial flagellar motor

The bacterial flagellar motor is a large macromolecular complex that exists in the cell wall of swimming bacteria. Its structure and function are discussed in Chapter 2. The flagellar motor is ion-driven, much like the F_O part of ATP synthase.

1.4 Bacterial motility

As with most behaviour in biology, bacterial motility is motivated by survival and reproduction. The advantage of being able to sense and respond to one's

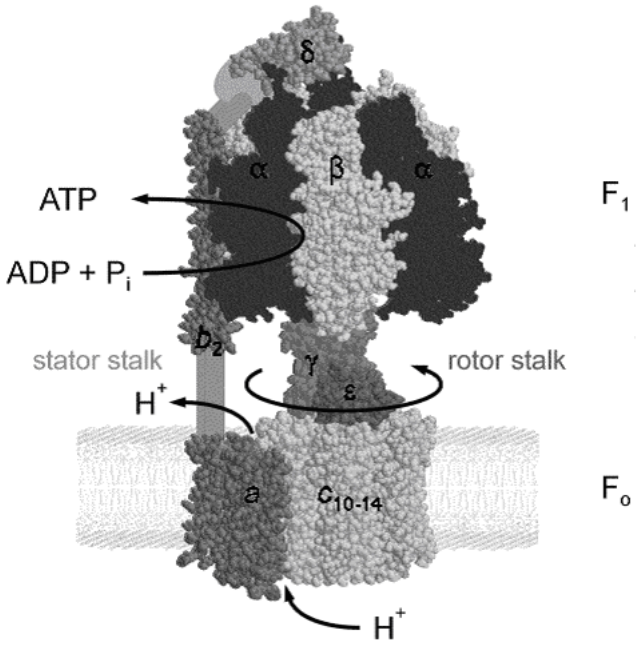

Figure 1.3: F_1F_OATP synthase. The membrane bound F_O is driven by the transmembrane proton gradient. The cytoplasmic F_1 is driven by ATP hydrolysis. Under normal conditions F_O drives F_1 in reverse, coupled by the common rotor stalk, to synthesise ATP. Figure adapted from Weber and Senior, 2003.

environment gives a crucial edge over the (now extinct) competition. Bacteria can sense a wide range of stimuli, for example changes in concentration of nutrients and toxins (Pfeffer, 1883), oxygen concentration (Engelmann, 1881), even the intensity and wavelength of light (Engelmann, 1883). Using these cues a bacterium can determine whether to stay put or move away, or hibernate or reproduce. Bacteria can also sense how many others are surrounding them and come to a collective decision, quorum sensing, of what behaviour to exhibit (Engebrecht et al., 1983).

Chemotaxis is the process that allows bacteria to move towards attractants such as a food rich environment and away from repellents such as toxins (Adler, 1973). In the case of *E. coli*, a species that swims with the use of multiple flagella, chemoreceptors present in the cell membrane activate a signal protein that alters the directional bias of the motor (Scharf et al., 1998). This system detects temporal gradients in nutrients such that the cell swims on average towards the nutrient (Section 1.4.2).

1.4.1 Types of motility

Most bacterial species are capable of motility either by swimming through liquid environments or by moving across surfaces. Types of motility are divided into six classes (Henrichsen, 1972). These descriptive classes of movement

are as follows.

Swimming Swimming is free three dimensional movement of bacteria in a liquid environment. Swimming is usually driven by the flagellar motor which rotates helical filaments converting rotary motion to forwards thrust. The number of filaments varies between species from single polar filaments (e.g. *V. alginolyticus* in a low viscosity environment) to bundles of four or more in *E. coli*. Swimming is the fastest form of movement with speeds reaching 150 μm per second (100 body lengths) (Magariyama et al., 1995) and is discussed in more detail in Section 1.4.2. Other forms of swimming exist with the spirochaetes swimming using internal flagella and cyanobacteria by an unknown, non-flagellar based mechanism (Pitta and Berg, 1995).

Swarming Flagellar filaments are also the driving force for bacterial swarming. Swarming can be thought of as a special case of swimming on a surface (Berg, 2005). When grown on a soft agar surface, cells produce flagella and move across the surface in a coordinated manner. Swarming is often used as an assay for motility.

Twitching Twitching motility is also known as social gliding or gliding with pili. Twitching is movement in short bursts, several micrometers at a time and usually only occurs when cells are close to one another on a moist

surface. Twitching involves the extension of rods (type IV pili) from the cell which are then retracted on contact with a surface to move the cell forwards (Skerker and Berg, 2001).

Gliding, sliding and darting Gliding without pili, also known as adventurous gliding is a smooth movement of cells on relatively dry surfaces. Cells usually travel along their long axis. This form of motility is poorly understood and there may be more than one mechanism involved (Harshey, 2003).

Sliding or spreading is not an active form of motility. Cells spread out due to the expansive forces created within a growing, dividing colony of cells.

Darting motility is where some cells are ejected from the colony. Nothing is known about the mechanism.

1.4.2 Flagellar based swimming

Swimming is the best understood of the forms of motility detailed above. It is the measurable output of the chemotaxis network (Wadhams and Armitage, 2004), providing those bacteria that exhibit it with a selective advantage over those that do not.

In species such as *E. coli* or *Salmonella*, the flagellar motor (Chapter 2) drives helical flagellar filaments, via the universal joint of the hook, either counter clockwise (CCW) or clockwise (CW). The pitch of the filaments

is such that when driven CCW they can group together to form a bundle and produce smooth straight line swimming (a run) but if driven CW are forced from the bundle causing the bacterium to tumble. A cartoon of these states is shown in Figure 1.4. This run and tumble mechanism results in a random walk for the bacterium allowing it to explore its three dimensional space. When the chemotaxis network detects that the bacterium is heading towards nutrients (or away from toxins) the CCW intervals are increased and the random walk becomes biased in that direction. Figure 1.5 shows an example of a random walk in two dimensional space with a uniform nutrient concentration and a biased random walk in a nutrient gradient. Extended runs when the cell is swimming towards nutrients (upwards) results in an average upwards swimming movement.

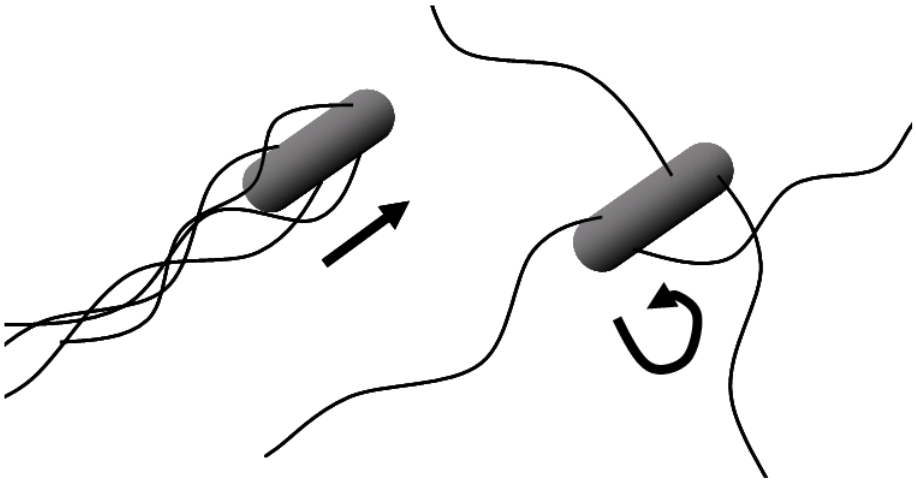

Figure 1.4: Cartoon of a peritrichously flagellated bacterium such as *E. coli* in smooth swimming (left) and tumbling (right) states. Changing the frequency of tumbling in response to external conditions allows the cell to bias a random walk towards nutrients.

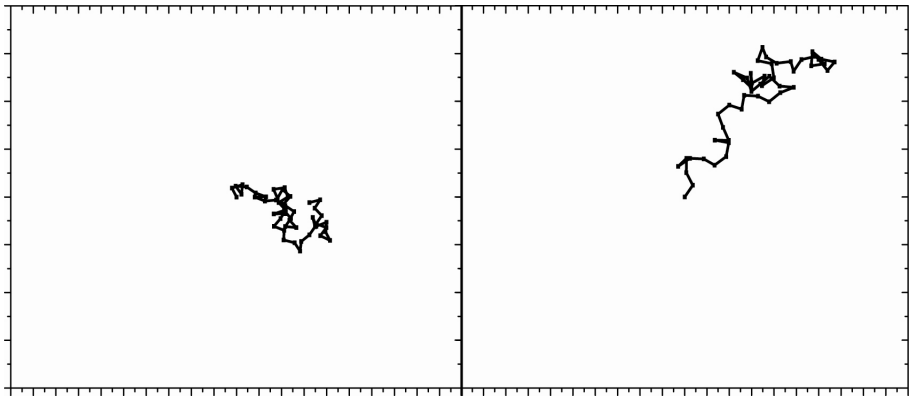

Figure 1.5: Illustration of a random walk and a biased random walk. In the biased random walk (right) smooth swimming events are longer in the upwards direction.

Chapter 2

The bacterial flagellar motor

The flagellar motor is, to quote Howard Berg, "A nanotechnological marvel." It is formed from multiple copies of about 20 different proteins, with a further 20 or so involved in its regulation and construction. As discussed in the previous chapter, it is the output organelle of the chemotaxis sensory system, allowing bacteria to search out more favourable environments. Much of the structure is known, although the membrane bound components remain more elusive. The exact nature of force production however is not fully understood, in particular how the torque-generating stator units interact with the rotor. This chapter reviews the current literature with regard to the structure, genetics, assembly and function of the flagellar motor, highlighting

recent results. The body of literature contributing to widely accepted ideas of the flagellar motor ranges from observation of swimming bacteria to the structure and dynamics of small parts of individual proteins. These ideas are drawn together and neatly summarised in recent reviews (Berg, 2003; Macnab, 2003; Blair, 2003; Berry, 2003) from which this chapter draws a lot of source material. Unreferenced statements summarising progress of individual topics are usually my interpretation of the consensus between these reviewers although primary literature is cited where appropriate.

Many of the structural and functional studies are performed using *E. coli*, *Salmonella* or *Vibrio Alginolyticus*. Whilst the number and arrangement of motors and filaments varies between species, the motor itself is a highly conserved structure. Differences do exist in the number of repeated subunits in various parts of the motor, but these are not thought to be crucial to understanding the mechanism. A recent paper (Murphy et al., 2006) has shown the structure of a complete flagellar motor within the membrane of *Treponema primitia*, however this species is a spirochaete with the flagellum contained between the cell membranes and the motor is much larger than those in *E. coli* or *Salmonella*.

2.1 Structure

Working from the tip of the filament back towards the cell body, the flagellar motor system consists of the filament cap, filament, junction proteins, hook, rod, adaptor and rotor. The L- and P-rings allow the rod to pass through the outer membrane and peptidoglycan and to rotate freely. The stator complex is anchored within the cell wall and interacts with the rotor (MS- and C-rings). A schematic of this arrangement is shown in Figure 2.1 and each part is described in more detail in the following paragraphs.

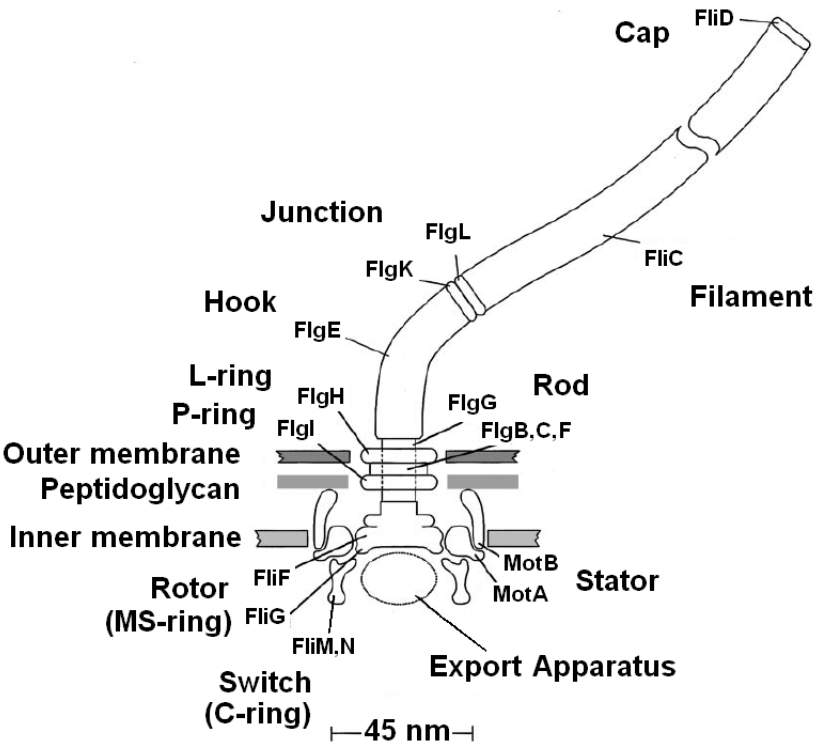

Figure 2.1: Diagram of the flagellar motor structure. The labeled parts of the motor are described in the text. The figure was adapted from Berg, 2003.

Filament and cap The filament cap consists of the protein FliD arranged in a pentameric structure. The cap rotates to allow flagellin subunits (FliC) to arrange themselves to form the filament beneath. There is a central channel in the growing filament that allows FliC to travel along the filament to the growing end. Filaments vary in length up to $\sim$15 μm consisting of tens of thousands of subunits but are only $\sim \frac{1}{40}$ μm in width. The filament consists of eleven protofilaments each with either a left or right handed "twist" arrangement of subunits. The subunit spacing between these twists is slightly different leading to long and short protofilaments, a mixture of which gives the final structure its characteristic helical shape. An atomic model of the filament is available (Yonekura et al., 2003) showing the central export channel and demonstrating the eleven fold symmetry. Figure 2.2 shows this model of the filament alongside a partial model for the hook (described below). The interaction with the cap has also been demonstrated (Maki-Yonekura et al., 2003). Sequence alignments across species, when compared to the available structure, reveal that while the central core of the filament is highly conserved, the outer regions are variable, a consequence of the evolutionary "arms race" between pathogenic bacteria and immune systems (Beatson et al., 2006).

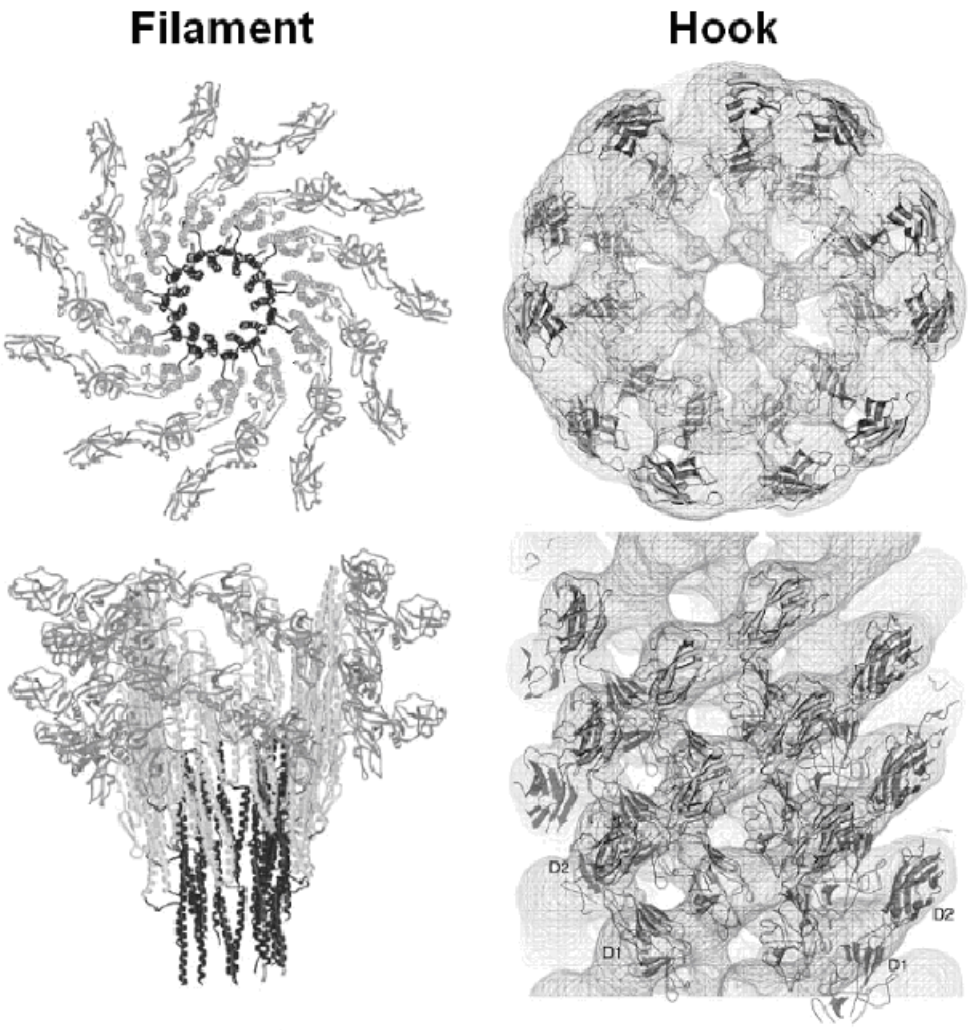

Figure 2.2: Ribbon diagrams of the atomic structure of the filament (left) and the docking of a partial atomic structure of the hook to cryo-elecron micrograph density maps (right). The eleven fold symmetry and central export channel can clearly be seen in both cases. The protofilament structure is clearer in the side on view of the hook. Figures were adapted from Yonekurea et al., 2003 and Samatey et al., 2004 respectively.

Hook and junction proteins About 130 copies of FlgE form the ∼55 nm long hook which has a similar structure to the filament. The hook is also formed from eleven protofilaments. In the hook the FlgE protofilaments can alter their arrangement between short and long allowing the hook to bend and act as a universal joint smoothly coupling the rotation of the motor to the filament.

A partial structure of the hook is known (Shaikh et al., 2005) and interactions responsible for operation as a universal joint have been identified (Samatey et al., 2004). The structure is shown in Figure 2.2 where x-ray crystallography of a fragment of the protein is superimposed on density maps from cryo-electron microscopy.

Junction proteins between the hook and filament FlgL (filament end), FlgK (hook end) are thought to act as structural adapters holding the filament in its rigid helical conformation but allowing transitions in the hook protofilaments for the universal joint action (Macnab, 2003). There are 11 copies of each adaptor corresponding to the 11 protofilaments of the hook and flagellum.

Rod, adaptor and rings The rod comprises FlgB, FlgC, FlgF, FlgG and transmits rotary motion through the cell membranes to the hook. These four proteins share structural characteristics with the hook and filament proteins,

probably arranged in a similar helical manner (Saijo-Hamano et al., 2004) with the export channel in the centre. FliE, also present in the rod structure is thought to be an adaptor protein connecting between the helical symmetry of the rod, hook and filament, and the circular symmetry of the rotor.

The L-ring in the outer membrane and P-ring in the peptidoglycan are composed of 26 copies of FlgH and FlgI respectively. These rings act as a bushing allowing torque to be transmitted by the rod structures through the peptidoglycan and outer membrane to the hook.

Rotor The rotor consists of FliF, FliG, FliM and FliN forming the MS- and C-rings. The structure of the MS-ring, consisting of FliF and FliG, reconstructed from single particle cryo-electron microscopy, reveals a 26 fold rotational symmetry (Suzuki et al., 2004) agreeing with previous estimates of protein number. The FliG-MotA interface is the site for torque generation.

FliM and FliN form the C-ring and together with FliG participate in the rapid CCW/CW switching of the motor. FliM also contains a binding site for CheY, the chemotaxis signaling protein that controls switching. The exact arrangement of proteins in the C-ring is not known but crosslinking studies and electron microscopy of the basal body (Lowder et al., 2005) (Paul and Blair, 2006) support the arrangement shown in Figure 2.3. The exact position of FliG remains to be resolved as these two methods give us slightly

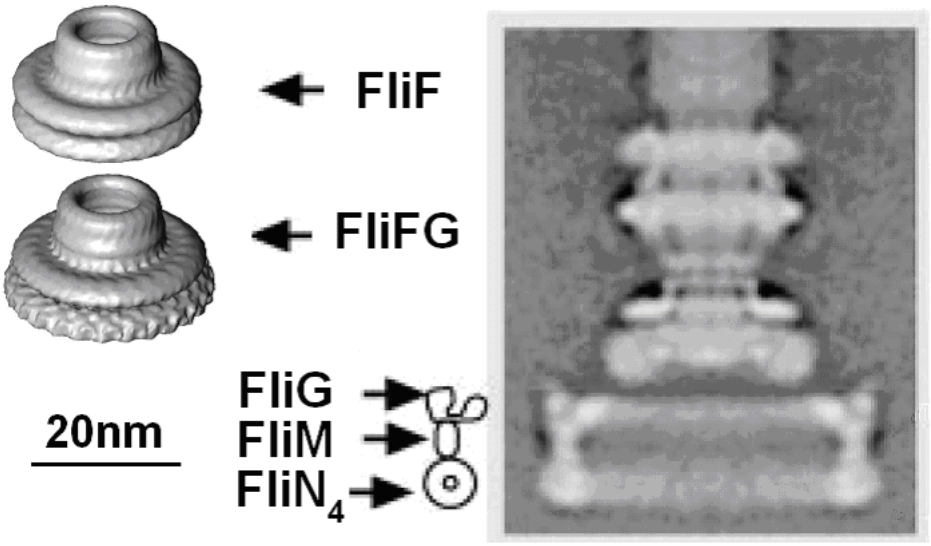

Figure 2.3: Reconstruction of MS ring and hypothesised arrangement of proteins in C-ring. The reconstruction (left) adapted from Suzuki et al., 2004, is on approximately the same scale as the electron microscopy of the basal body (right) adapted from Paul and Blair, 2006. It is not clear whether FliG is part of the MS- or the C-ring with single particle reconstructions and crosslinking studies differing in opinion.

different results.

Stator The stator units comprise the proteins MotA and MotB (PomA and PomB in sodium motors). Each stator contains four copies of MotA and two copies of MotB forming two ion channels per unit (Braun and Blair, 2001). Crosslinking studies (Braun et al., 2004; Kojima and Blair, 2004) have shown that the transmembrane helices of MotA and MotB are arranged as shown in Figure 2.4.

Stator units are situated around the rotor, attached to the peptidoglycan via the peptidoglycan binding domain (PBD) of MotB. There are at least 11 of these in a full *E. coli* motor as initially observed by freeze fracture electron microscopy (Khan et al., 1988) and now confirmed by experiment (Chapter 4).

2.2 Genetics

The genetic arrangement and regulation of flagellar motor genes is logical and tightly controlled (Armstrong and Adler, 1969; Pruss and Matsumura, 1997). The assembly of the motor (Section 2.3) requires parts of the motor to form before others can. The regulatory system associated with the flagellar genes ensures that parts are not synthesised until they are required.

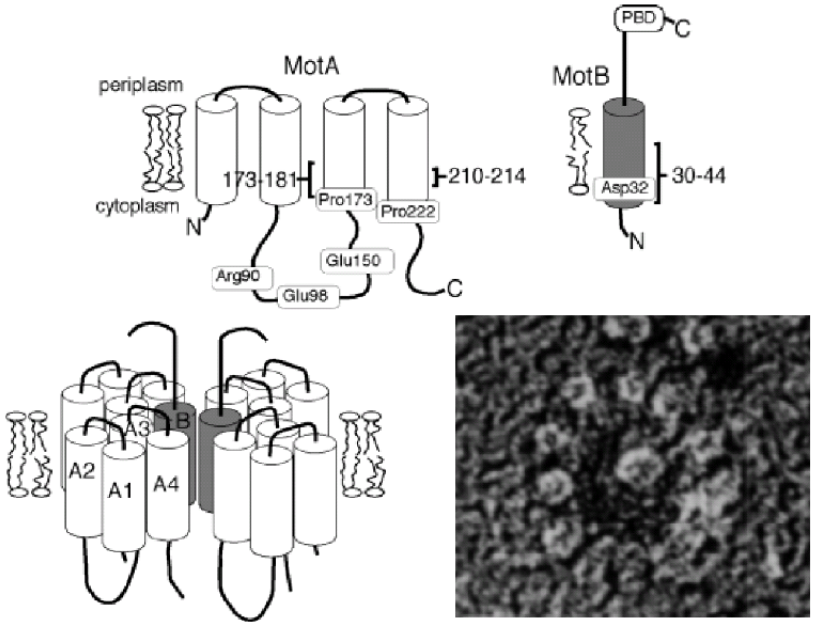

Figure 2.4: Transmembrane helices of MotA and MotB and their hypothetical arrangement into the torque generating complex. Residues with a role in torque generation are labeled. Also pictured is an example of studs due to torque generators, arranged around the central rotor, as observed by freeze fracture electron microscopy. Figures were adapted from Braun et al., 2004 and Khan et al., 1988 respectively.

Flagellar synthesis is controlled by the master operon *flhDC*. Expression of these genes is required for the expression of all other flagellar genes. FlhDC levels are intimately linked to the cell division cycle and the starvation state of the cell as well as a variety of other cellular systems. Expression is also stimulated by *fliA* (a class 2 gene sigma factor stimulated by FlhDC) resulting in a positive feedback system to maintain flagellar synthesis once started.

The *flhDC* group of genes is known as the class 1 operon. The other operons controlling flagellar synthesis and operation are organised into classes 2 and 3. The class 2 operons contain genes encoding the main body of the motor consisting the rotor, L-, P-, MS- and C-rings the rod and the hook. Also in class 2 are the genes for the export apparatus responsible for the organisation and control of extracellular synthesis. Expressed with the class 2 operons is *flgM* which prevents expression of class 3 operons.

On completion of the hook, the export apparatus pumps FlgM out of the cell allowing expression of the class 3 operons (Hughes et al., 1993). These code for the filament and the torque generating units but also for chemotaxis receptors and signaling proteins. This class arrangement and regulation ensures that flagellar synthesis is an efficient, ordered process. Fluorescent reporter strains demonstrate this ordered expression (Kalir et al., 2001) (Figure 2.5) which has also been expressed as a mathematical model (Kalir and Alon, 2004).

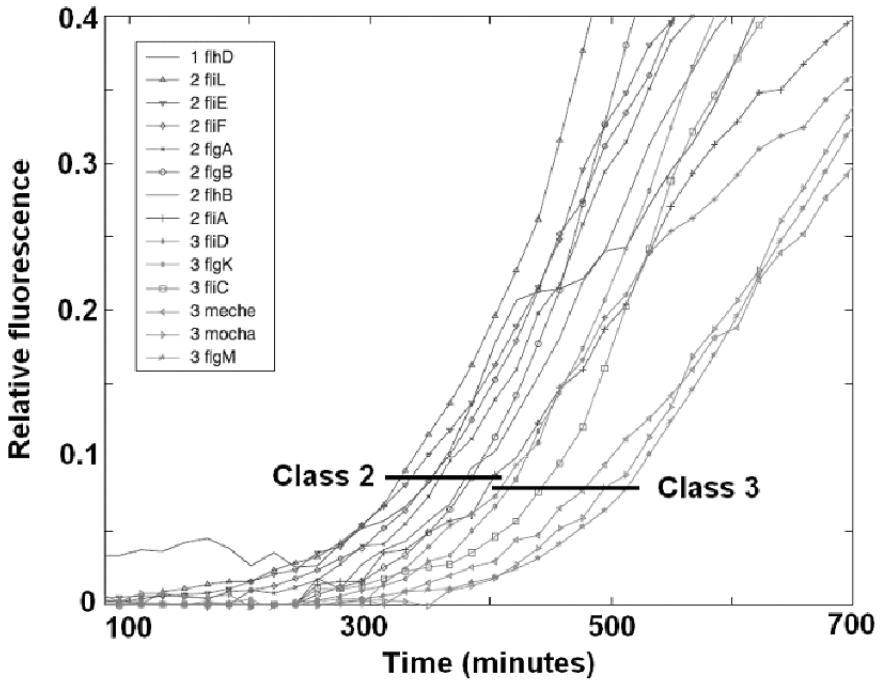

Figure 2.5: The expression order of flagellar genes as measured by fluorescent reporter strains. The order of expression is tightly regulated such that components of the motor are not produced until they are required. Class 2 genes are all expressed before Class 3. Figure adapted from Kalir at al., 2001.

2.3 Assembly

Flagellar motor assembly is closely linked with the genetic arrangement (Section 2.2) with parts synthesised as and when they are required. Three assembly mechanisms are utilised during the assembly. The first is the targeting of proteins to the membrane via the Sec pathway. This pathway employs chaperone proteins that recognise signal peptides in the target protein and assist with insertion into the membrane. Once in the membrane the proteins can fold to their native conformation. The second mechanism is self-assembly. Once the proteins are in the correct location and conformation they can spontaneously assemble into the required complex. The third mechanism is type III secretion through the export apparatus. The main body of the flagellar motor functions as a pump driving monomers down the narrow central channel which then assemble to form the outer parts of the motor.

The first parts of the motor to be formed are the MS-ring and export apparatus. Multiple copies of FliF are escorted to the membrane where they self assemble into the ring structure. The C-ring and export apparatus then form around this structure. The export apparatus shares homologies with the type III secretion systems used by bacteria such as *Salmonella* to inject virulence factors into target cells.

On completion of the rotor and export apparatus it is now possible for

the axial components to be assembled via the export apparatus and for the stator units to associate with the rotor. Given the genetic arrangement and regulation it is likely that the stator units are not formed and positioned until after the hook has been completed. The stator units assemble in the membrane finding the rotor by diffusion. Resurrection experiments (Block and Berg, 1984; Blair and Berg, 1988) show that stator units can be added after the rest of the motor has been completed and recent results (Leake et al., 2006) indicate that units are exchanged on a fairly rapid timescale during motor operation. Purification of the torque generating complex (Braun and Blair, 2001; Sato and Homma, 2000) shows that the complex exists in the membrane, separate from the motor. Chapter 4 discusses the incorporation of units into the motor in light of additional experimental observations.

Components for the rod are exported and assembled through the rotor with the driving force provided by ATPase activity in the export apparatus. FlgJ is a rod capping protein that contains a domain capable of digesting the peptidoglycan layer allowing the formation of the rod up to the outer membrane. Once the rod has reached this stage the L- and P-ring proteins are exported via the Sec pathway and assemble around the rod and the beginnings of the hook.

The hook is assembled underneath the hook cap which prevents loss of the hook protein to the surrounding medium and catalyses assembly. The length

of the hook is tightly controlled. The exact mechanism of control is not known although the protein FlgK is important and the export apparatus may also have a role. A model where hook length is controlled by a transition between a secretion limited and diffusion limited rate of export has been proposed (Keener, 2005) though there is no direct evidence for this mechanism. The junction proteins are then exported in order before the filament cap is added. The filament forms underneath the cap to produce a fully formed flagellar motor.

2.4 Function

Active proteins The proteins active in flagellar rotation have been identified via mutational studies as MotA, MotB, FliG, FliM and FliN. Mutations in these genes result in fully formed but non-functional flagellar motors. As discussed in Section 2.1, MotA and MotB form the stator units and FliG, FliM and FliN form the rotor and are active in switching of the motor.

Torque-generating units The MotAMotB (PomAPomB in sodium motors) complex forms two ion channels (Figure 2.4) within which mutations of a critical charged residue (Asp32 on MotB) block motor function. The PomAPomB stator complex of *Vibrio* has been shown to function as an ion

channel when reconstituted into proteoliposomes (Sato and Homma, 2000) but this has yet to be shown for the MotAMotB complex. Much of the research focus on the MotAMotB complex has been on the arrangement of the transmembrane segments (Section 2.1, Stators) in order to deduce the mechanism for torque generation.

Rotor-stator interaction MotA contains charged residues that interact with the rotor and are important, although no single one is essential, for motor function. It is hypothesised that a conformational change in MotA, induced by ion passage through the channels, drives the rotation (Kojima and Blair, 2001). These charged residues are not as important for rotation in the sodium motors of *Vibrio*. This may be due to the presence of the additional MotX and MotY proteins as these charged residues in sodium stators, adapted to work with *E. coli*, were once again essential (Yakushi et al., 2006). Biochemical studies of the MotAMotB complex provide some insight into the mechanism of torque generation at the protein level. However physical experiments with functioning motors generate useful information that can be used to further elucidate this mechanism.

Torque speed relation Forced rotation of the motor, or application of different viscous loads, allows the torque-speed curve to be plotted. Originally

by electro-rotation of tethered cells (Berg and Turner, 1993), more recently by variation of the viscosity of the medium with speeds measured by beads attached to filaments (Chen and Berg, 2000), the torque speed curve of *E. coli* shows a characteristic shape as illustrated in Figure 2.6. At room temperature the torque follows a shallow linear decrease up to a knee speed of $\sim$ 200 Hz then drops rapidly to zero around 300-350 Hz. This characteristic shape is also seen in motors with lower numbers of torque generators (Ryu et al., 2000) and in the sodium driven motor of *Vibrio* (Sowa et al., 2003). The shape is more indicative of a powerstroke mechanism, where the energy from ion transit is coupled directly to rotation, rather than used to rectify a Brownian ratchet. This supports the biochemical evidence for a conformational change in MotA.

The number of torque generators The number of torque generators present in a motor can vary. Early work (Block and Berg, 1984; Blair and Berg, 1988) suggested that the maximum number of torque generators in a motor was eight and that wildtype numbers were lower. However this was not consistent with the number of studs (thought due to MotB) observed in freeze fracture electron microscopy (Khan et al., 1988). This number was also inconsistent with studies where motors were disrupted either mechanically (Berry et al., 1995), electrically (Fung and Berg, 1995) or electrochemically

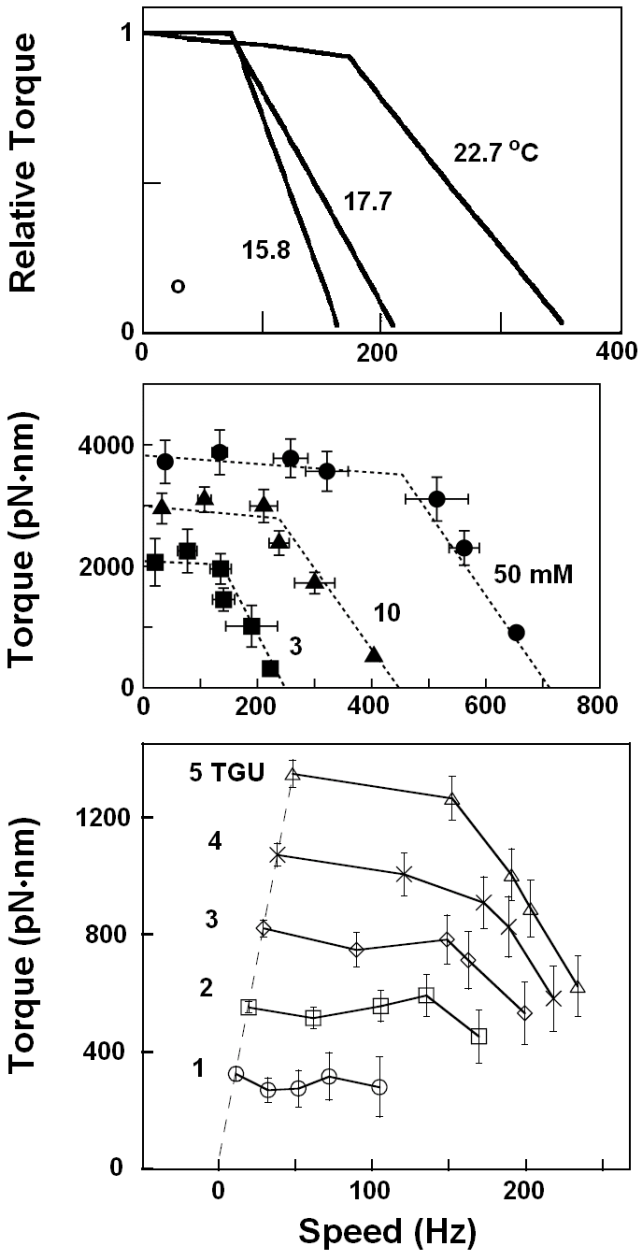

Figure 2.6: The measured torque speed relation at different temperatures in the proton-driven flagellar motor, at different sodium concentrations in the sodium-driven motor and at different numbers of torque generator in the proton-driven motor. The same characteristic shape is observed in all cases. Figures were adapted from Chen and Berg, 2000, Sowa et al., 2003 and Ryu et al., 2000.

(Sowa et al., 2005) and equal speed increments of less than one eighth maximum speed were observed. It is now clear that there can be at least 11 units in a full motor (Reid et al., 2006), (Section 4.4). The number of torque generators has implications for the overall energy balance of the motor and the assumption of independent units. These issues are discussed in Chapter 4.

Stepping The proposed mechanism for rotation, mediated by a conformational change in MotA applying an increment of torque to the rotor, results in a stepping motion. The observation of steps is complicated by the elastic linkage via the hook to the filament (and attached bead) where rotation is observed. Recently these steps have been observed in extremely slow hybrid sodium motors in *E. coli* where the speed was reduced either by removal of the sodium motive force or by cumulative photodamage (Sowa et al., 2005). The steps showed a periodicity of 26 consistent with FliG on the rotor. These experiments relied on transient state motors and it is necessary to extend these results by observation of stable motors in order to deduce more detailed information about the function of the motor. Progress towards this goal is detailed in Chapter 5.

Switching The directional bias of the motor is controlled by the chemotaxis signalling protein CheY. Phosphorylated CheY (CheY-P) binds to FliM on the rotor inducing the direction change. The direction change is rapid and does not proceed via intermediate speeds[1] indicating that the change is within the rotor rather than individual torque-generating units. The bias is sigmoidally dependent on the amount of CheY-P present indicating a cooperative effect at work. An Ising model, where transitions in FliM are catalysed by CheY-P binding and cooperative effects between neighbours stabilise transitions, correctly describes the equilibrium switching behaviour (Duke et al., 2001). Recent experiments also show that this model can reproduce the underlying dynamic behaviour (Korobkova et al., 2006).

Switching is also shown to be dependent on the motor load with CW (tumble) rotation more likely at high loads (slow speed) (Fahrner et al., 2003). This result suggests the switch complex may be able to sense motor speed perhaps by proton flux. The dependence of switching on torque generator number is discussed in Chapter 4.

Driving force The flagellar motor is powered by the proton-motive force (pmf), or in some cases the sodium-motive force (smf) across cell membranes. Ions passing into the cell, through channels formed by the torque-generating

[1]Work is currently in progress in our lab to investigate this on shorter timescales.

units, drive rotation of the motor in either direction. Simultaneous measurement of both slow rotating (high viscous load) and fast rotating (low viscous load) motors during de-energisation with ionophores have shown that the motor speed is linear with pmf over the full speed range (Gabel and Berg, 2003). This confirmed earlier results where cells were energised with an external voltage (Fung and Berg, 1995). The effect of altered pH is more difficult to ascertain experimentally as the cell has many systems devoted to regulation of intracellular pH. However it has been shown that lowering internal pH disrupts motor function (Minamino et al., 2003). A more useful probe for the concentration gradient exists with sodium-driven motors, where the concentration of internal sodium is not as tightly regulated. Under these conditions motor speed is approximately linear with sodium motive force (Lo et al., 2006).

The absolute flux of ions through the proton-driven motor is only ~ 1 % of the total membrane proton flux. The only measurement of this flux was with *Streptococcus* (Meister et al., 1987). Proton uptake was measured from the change in pH of the bulk medium and rotation dependent flux by the change in this quantity on crosslinking of flagellar filaments. The uncertainty in this measurement was large with estimates between 970 and 1440 protons per motor per revolution. Estimates of proton flux based on the torque delivered by the motor are discussed in Chapter 4.

2.5 Models

Models for the mechanism of rotation in the bacterial flagellar motor are widely varied. Tight binding or loose, channel, cross-bridge or electrostatic, turnstile or turbine (Berg, 2003; Berry, 2000), also an ion channel inspired helix rotation model (Schmitt, 2003). In each model ion transitions either directly or indirectly generate rotation in the motor. These models differ in mechanism but what any model must do is reproduce the experimentally obtained data, the most important and difficult to generate part being the torque-speed curve. It has recently been shown that there are four essential assumptions required for any model that correctly reproduces this data (Xing et al., 2006).

1. Rotation of the motor is observed through a soft elastic linkage between the motor and the viscous load. These elastic linkages are experimentally observed in both the hook and the MotB peptidoglycan binding domain.

2. Motor rotation and ion transport are tightly coupled. This explains the experimental observation of the linear speed-pmf relation.

3. The power stroke is driven by a conformational change in the stator due to proton binding/unbinding.

4. The ion channel through the stator is gated by the motion of the rotor.

These four assumptions, each based on experimental evidence, correctly reproduce the behaviour of the motor. The exact mechanism of torque generation remains open to debate.

Chapter 3

Experimental techniques

A number of questions surround the area of detailed function of the motor. To address these, experimental techniques must be able to accurately measure the rotation of the motor, both position and speed. Single molecule techniques are essential to extract information about the operation of an individual motor and provide more information then averages such as swimming speed, often the output of more than one motor, or swarming behaviour, the result of a growing colony.

3.1 Cells and cultures

To investigate torque generation in the motor, strains of *E. coli* were chosen or developed to allow control of the expression of torque generating units. The proteins MotA and MotB form the torque-generating unit (Chapter 2) that acts as an ion channel and interacts with the rotor to produce motion. The strains developed contain either mutations or deletions in these genes with controllable induction of either the WT proton-driven units or a chimeric sodium-driven unit. These strains were cultured under conditions favourable for motility and the motor rotation observed.

3.1.1 *E. coli* Strains

There were four strains of *E. coli* used in this work. Strains are summarised in Table 3.1 and detailed in the text below.

All strains used were pilA-minus (pili are used in twiching motility, Chapter 1) rendering the strains non-pathogenic and less sticky to reduce the interaction between cell bodies and rotating beads. Strains were also filament-minus with a sticky filament allele (Kuwajima, 1988) carried on a plasmid. The sticky filament allele contains an exposed hydrophobic patch allowing easy attachment of hydrophobic species (e.g. latex beads). This allele also weakens the filament allowing it to be easily sheared.

Strain/plasmid	Relevant genotype/phenotype	Reference
Strains		
"MotA"	HCB1271, pDFB36, pFD313Cm	(Ryu et al., 2000)
"MotAB"	YS34, pDFB27, pFD313Cm	(Reid et al., 2006)
"Chimera"	YS34, pYS11, pYS13	(Sowa et al., 2005)
"WT"	KAF95, pFD313	(Berg and Turner, 1993)
HCB1271	*fliC*::Tn10 pilA'-Kn^R *motA448*	(Ryu et al., 2000)
YS34	*fliC*::Tn10 ΔpilA Δ*motAmotB* Δ*cheY*	(Sowa et al., 2005)
KAF95	Δ*cheY fliC726*	(Berg and Turner, 1993)
Plasmids		
pFD313	fliCst, Ap^R	(Kuwajima, 1988)
pFD313Cm	fliCst, Cm^R	(Ryu et al., 2000)
pDFB27	P_{ARA} *motAmotB*, Ap^R	(Blair and Berg, 1988)
pDFB36	P_{LAC} *motA*, Ap^R	(Blair and Berg, 1988)
pYS11	fliCst, Ap^R	(Sowa et al., 2005)
pYS13	P_{LAC} *pomApotB*, Cm^R	(Sowa et al., 2005)

Table 3.1: Strains and plasmids.

"MotA" The MotA strain carries a point mutation in the *motA* gene on the chromosome rendering the strain non-motile. The strain carries two plasmids. The first contains wild type *motA* under the lac promoter allowing controllable induction of the torque-generating unit protein MotA. The second carries the sticky filament allele. This strain was previously used to measure the duty ratio of the torque-generating units (Ryu et al., 2000).

"MotAB" The MotAB strain has both *motA* and *motB* genes deleted. The strain carries wild type *motAmotB* under the ara promoter allowing controllable induction of the torque-generating unit proteins MotA and MotB and also carries the sticky filament plasmid. This strain was developed[1] for the work in Chapter 4 and published in PNAS (Reid et al., 2006).

"Chimera" The Chimera strain is similar to the MotAB strain but carries sodium-driven *pomApotB* under the lac promoter rather than proton-driven *motAmotB*. This strain was used to observe stepping in the motor (Sowa et al., 2005).

"WT" The WT strain has no mutations or deletions in either *motA* or *motB* and carries the sticky filament plasmid. This provides a useful comparison of how a naturally occurring motor would behave under the experi-

[1]Strain was made by JC and myself

mental conditions applied. This strain was originally used in electro-rotation experiments (Berg and Turner, 1993).

3.1.2 Experimental culture

Stock cultures of each strain were prepared by growing up a saturated culture over 24 hours at 30 ^{o}C with shaking in tryptone-broth (1% tryptone, Difco; 0.5% sodium chloride) containing the appropriate antibiotics, either 100 μg ml^{-1} ampicillin, 34 μg ml^{-1} chloramphenicol or both, to preserve the plasmids. 10 % dimethylsulfoxide (DMSO) or two parts in five of 50 % glycerol was added as a cryoprotectant and 100 μl or 200 μl aliquots respectively were frozen and stored at -80 ^{o}C.

For an experiment one aliquot was added to 5 ml tryptone-broth with appropriate antibiotics and inducer and incubated at 30 ^{o}C with shaking. Typical incubation times were between 4 and 6 hours (Optical density at 600 nm $\sim$0.3 cm^{-1} for WT and MotA, $\sim$1 cm^{-1} for MotAB and Chimera) at which point cells are observed to swim or tether and spin when dropped onto a microscope slide.

3.2 Measurement of motor rotation

This section describes the acquisition of raw data from an experimental culture. In the case of tethered cells the angle of the whole cell determines motor angle. For bead assays the bead position determines the motor position. Further data processing, including extracting speeds from these data, are described below.

When analysing data it is important to understand exactly how the information is collected and recorded and possible sources of error that may arise especially when pushing methodologies to their limits. For example it is possible that events may be missed or artefacts introduced because of the choice of collection method and initial analysis. With this in mind the limitations and potential pitfalls of each method are discussed where possible.

3.2.1 Slide preparation

Common to all the experiments is the preparation of a tunnel slide. The tunnel allows a surface to be prepared, cells added and the excess washed away leaving a sparse covering of cells upon which single motor experiments can be performed.

The tunnel slide The tunnel slide consists of a standard microscope slide, two pieces of double sided sticky tape and a coverslip. The gap formed between the coverslip, slide and two edges of the tape forms a tunnel $\sim$ 100 μm high with a typical volume of less than 10 μl. Solutions are wicked through this tunnel using a tissue to prepare the slide for measurements. 100 μl of solution was more than enough for complete exchange of medium.

Washing and shearing To produce short filament stubs for either tethering or bead attachment, cells were passed through narrow gauge needles up to 60 times (Chen and Berg, 2000). Long filaments were sheared off by the hydrodynamic forces applied. Cells were then washed in a motility medium (10 mM potassium phosphate; 0.1 mM EDTA; pH 7.0) to remove the free filaments and prevent regrowth.

Tethered cells Cells added to a "dirty" coverslip tunnel slide, where the coverslip was straight from the box and not KOH-cleaned (see next paragraph), can attach by their filament stubs. If there is only one attachment to the slide, the whole cell body rotates about the axis of this motor (Silverman and Simon, 1974). The rotation of tethered cells is monitored by video.

Bead assay In a bead assay the rotation of a bead about a motor is monitored rather than the rotation of the cell body (Ryu et al., 2000). This

gives a consistent viscous load on the motor under observation compared with the variable viscous load of a cell body that can have a range of sizes and tethering points.

Before construction of the tunnel slide, coverslips were cleaned in a saturated solution of potassium hydroxide in 95 % ethanol (KOH-cleaned) to create a negatively charged hydrophilic surface. Poly-L-lysine is flushed through the tunnel first, then washed out leaving a positively charged monolayer bound to the coverslip. This charged layer immobilises the (negatively charged) cell bodies when they come into contact.

Excess cells are washed away before beads are flushed through the tunnel, either plain (Polysciences) or fluorescent (Invitrogen Molecular Probes) polystyrene latex beads of a given size. Excess beads are then flushed away and the slide is ready for observation using either back-focal-plane detection or fluorescence. Fluorescent beads had a sulfate surface modification to ensure attachment to filament stubs.

In the case of resurrection experiments, the final motility buffer was supplemented by inducer (either IPTG[2] or arabinose) and 5 % T-broth to enable protein production.

[2]Isopropyl-β-D-thiogalactopyranoside

3.2.2 Video analysis of tethered cell rotation

A variety of methods exist to monitor the rotation of tethered cells. Several papers (Berg and Turner, 1993; Samuel and Berg, 1995) have used linear graded filters which produce an oscillating signal as a cell rotates in the field of view. The simplest method involves timing revolutions during video playback (Block and Berg, 1984).

This section describes a simple method that does not require specialised optics and retains more information than simply timing and counting revolutions. An added advantage of this method is that several cells can be recorded concurrently in one video sequence then separated and analysed independently. The analysis is also free from user interaction eliminating any bias that may be introduced.

Video format and capture The experiment is recorded on a standard VHS device taking the output from a CCD camera (for details of the microscope see Section 3.2.3). The video signal is captured by a desktop PC at either 25 Hz interlaced frames or 50 Hz fields. These are equivalent as the interlaced signal consists of two sequential fields. The first step in the analysis is to separate the fields (if required) and to note that the number of pixels in the vertical direction is halved as a result. It should also be noted that two consecutive fields do not show exactly the same view due to the

interlacing and must therefore be shifted by half a pixel in the vertical direction (a quarter each field in opposite directions). This is necessary as our measurements will be very sensitive to the centre of the object. The video data is now in a useable format at 50 Hz suitable for our experiments where cells spin up to about 20 Hz.

Extracting angle data Video analysis is performed using the IMAQ add on package for LabView (National Instruments). Figure 3.1 shows the image processing steps required to extract the angle of the cell. Best results were obtained with the focus such that cells appear dark on a light background in brightfield imaging (a). The image is inverted (b) and the background subtracted (c) as estimated by pixels at the extremes of the image. This background correction is crude but sufficient to threshold the image and segment the cell as a binary object (d). Calculating the centre of mass of this object for each image produces a circular trace from which angle and speed can be extracted (Section 3.3).

3.2.3 Back-focal-plane detection of latex bead position

Back-focal-plane detection was used to obtain the data for Chapter 4. The light scattered by an object, in this case a latex bead, within a weak optical trap is detected in order to deduce the position with nanometre precision

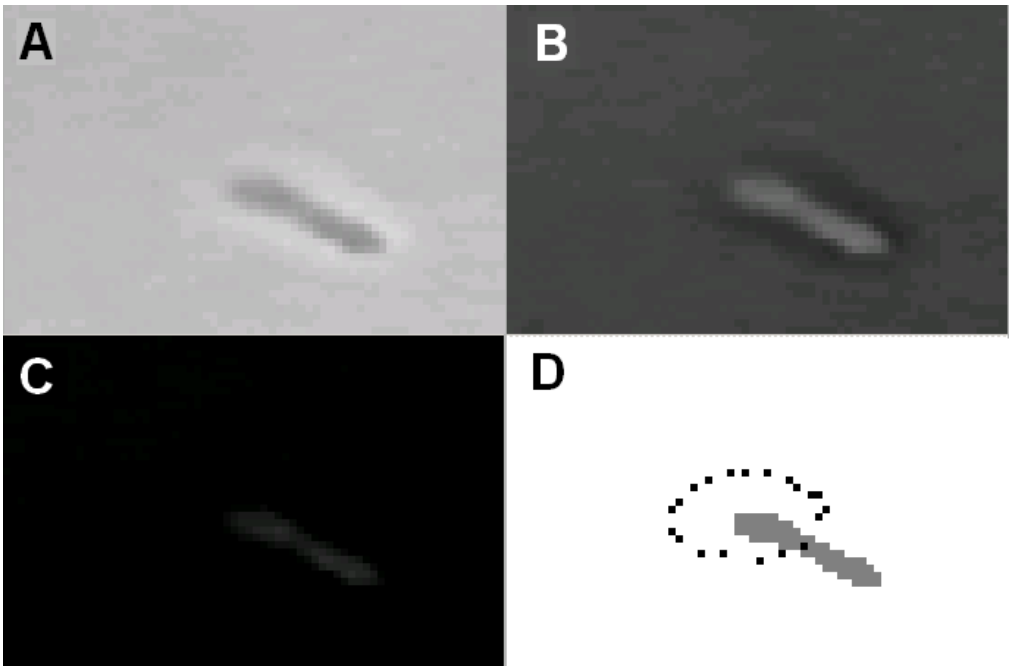

Figure 3.1: Video analysis of a tethered cell. The image is inverted, background corrected and thresholded to produce a binary image of the cell. The centre of mass of the binary object describes an orbit from which the speed can be calculated. The orbit appears flattened due to the reduced number of horizontal lines from capturing fields.

(Gittes and Schmidt, 1998).

Back-focal-plane detection theory

Laser trapping A refractive particle can be confined in three dimensions by a focused laser in an optical trap. The forces on a trapped particle as modeled by ray optics (particle larger than the wavelength of light) are illustrated in Figure 3.2. In the x-y plane, any displacement of the particle results in refraction of the beam and thus a change in the momentum of the photons passing through the particle. The resultant force on the particle acts to restore it to the centre of the beam. A steeply focused beam, through a high numerical aperture objective, provides enough force to confine the particle in the z-direction (beam direction) as well. Similar restoring forces are present when the particle is smaller than the wavelength of light and Rayleigh scattering, rather than ray optics is the appropriate model.

Position detection The position of a particle in the x-y plane can be measured by observing the beam in the back-focal-plane of the condensing lens. As the beam passes through the sample it is altered, the change in the photon momentum being equal and opposite to the trapping force on the particle (conservation of momentum). In the ray optics limit, the displacement of the particle alters the angle light enters the condenser. For small particles,

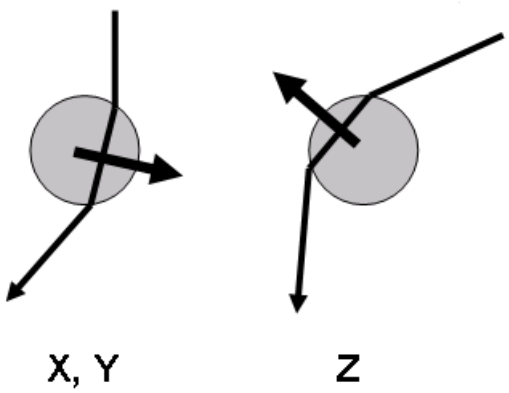

Figure 3.2: Ray optics model of laser trapping. Refraction of the incident laser light generates a restoring force to the trap centre in both the x-, y- and z-directions for a tightly focused beam.

a far field interference effect produces a similar result. A quadrant photodiode placed in the back focal plane of the condenser detects the change in the beam producing a signal proportional to the particle displacement. The photocurrents from the four quadrants a, b, c and d (clockwise from top left) are used to calculate the x and y displacements as follows,

$$x = \alpha \frac{(b+c)-(a+d)}{a+b+c+d},\ y = \beta \frac{(a+b)-(c+d)}{a+b+c+d},$$

where α and β are calibration constants.

Experimental setup

A diagram of the detection setup is shown in Figure 3.3. The apparatus was constructed by Alex Rowe and Richard Berry (Rowe et al., 2003). Brightfield

illumination is provided by a fibre coupled tungsten halogen bulb with short wavelengths blocked by a green filter to prevent damage to the biological specimen. Light is focused by the condenser lens. The sample is imaged by the oil immersion objective (100x) and projected onto the CCD camera via a zoom lens.

The trapping beam was from a 1064 nm diode pumped solid state laser. The beam was attenuated by a half waveplate and polariser and expanded to fill the back aperture of the high numerical aperture (NA 1.4) objective. The beam was typically less than 2 mW at the back aperture to prevent damage to the specimen, not strong enough to trap but adequate for detection. The trapping beam was coupled and decoupled from the optical path, traveling antiparallel to the illumination, via dichroic mirrors. The beam was re-collimated by the condenser lens and the back-focal-plane of the condenser projected to fill the surface of the quadrant photodiode. Ambient light was blocked from the photodiode with a long pass (1000 nm) filter.

The sample was mounted on a piezo electric stage to allow fine position control. The stage and optics were bolted firmly to an air table to reduce vibrations and drift.

The signal from the quadrant photodiode was sampled at 2 kHz to a desktop PC. To reduce drift in long measurements the mean position of e.g. 1 s of data was used in a feedback loop to the piezo stage to keep the

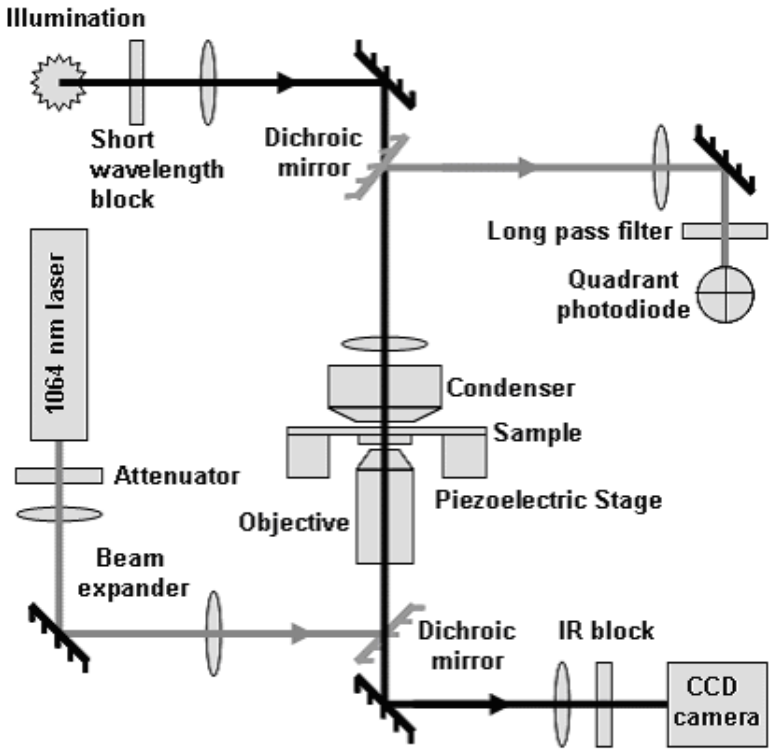

Figure 3.3: Important components in our back-focal-plane detection system. Laser paths are shown in gray with light paths in black. The function of the components are described in the text.

bead under observation central in the trap. Feedback was only necessary for measurements lasting several minutes or longer.

Calibration

In order to accurately determine the viscous drag of a bead rotating on a flagellar stub it is necessary to know the radius of its orbit as well as the bead size. The signal on the quadrant photodiode was highly dependent on the z-position of the bead in the trap. A free floating 1 μm trapped bead appeared white while a bead below and above the trap (and the brightfield focus) appeared black or fuzzy white respectively. The best experimental signal was usually obtained with the bead somewhere between white and fuzzy white. These two limits were used to calibrate position and quadrant photodiode reading.

Figure 3.4 shows the mean positions, each of 1 second of data, when a 1 μm diameter stuck bead is moved in a 0.2 μm radius circle (8 points at 45^o intervals) at these two limits. This is typical of an experiment. The average radius of the signal was 0.25 ± 0.03 giving a calibration constant of 0.8 ± 0.1 μm. We see firstly the difference in signal for a small change in z, secondly that the x- and y-calibrations are slightly different and thirdly that the quadrant diode is slightly misaligned with the piezo stage. These uncertainties will contribute to the error in our estimate of the frictional drag

coefficient of a bead. In an experiment the laser will also pass through the cell body which will distort the detection signal and must be considered when making quantitative judgments.

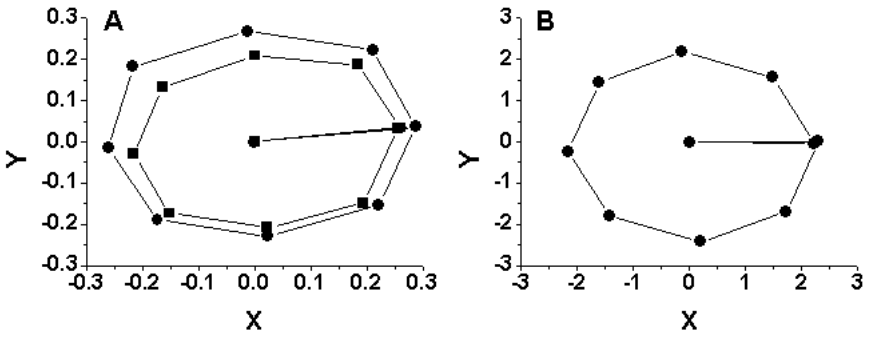

Figure 3.4: (a) Calibration of the back-focal-plane detection system. Signals for a bead around a 0.2 micron circle are taken in typical experimental conditions. The difference for a slight change in bead z-alignment is observed. (b) Calibration of the fluorescent bead detection system. Positions for a bead moved in a 0.1 micron circle were measured in pixels.

3.2.4 Fluorescent bead position detection

There are a number of advantages to using fluorescent bead detection as opposed to back-focal-plane laser microscopy. The image analysis is linear, giving more confidence that the detected position is the true position of the bead. It is also possible to use a smaller bead and therefore observe the motor under a lower load condition, closer to that of its native operation[3]. Fluorescent bead detection was used to collect data for Chapter 5.

[3]Smaller beads can be used in back-focal-plane detection to approach these conditions however it is difficult to extract exact positions.

Fluorescence microscopy relies on materials that absorb light at one wavelength (excitation) then release the energy at a different wavelength (emission). The emitted light allows one to observe objects much smaller than the resolution limit of the microscope, down to single fluorescent molecules if required.

A small object, for example a fluorescent bead, is imaged as the point spread function of the microscope convoluted with the image of the bead. Whilst the spread of this image is much larger than the displacements we wish to measure, its centre can be accurately located giving us the required spatial resolution.

Experimental setup

The basic setup is similar to the optical trap setup. Brightfield illumination was provided via a fibre coupled lamp and imaged onto a CCD camera. Fluorescent illumination was provided by a collimated laser the wavelength of which depended on the fluorescent properties of the bead. Two types of bead were used: yellow/green excited by a 488 nm argon ion laser and crimson beads excited by a 633 nm HeNe laser. The collimated laser beam was attenuated by neutral density filters to provide optimum illumination. A field iris reduced the area illuminated. The laser was directed into the sample via a filter cube which allowed the excitation wavelength into the

sample but prevented it from passing back to the detector. A diagram is shown in Figure 3.5. The apparatus was constructed by Mark Leake and Richard Berry (Leake et al., 2006)

During a fluorescent measurement the brightfield illumination was blocked off and the imaging path switched to a low light, high frame rate electron multiplying CCD camera (EMCCD). Images consisted of a 16 × 16 pixel grid capturing the bead rotation.

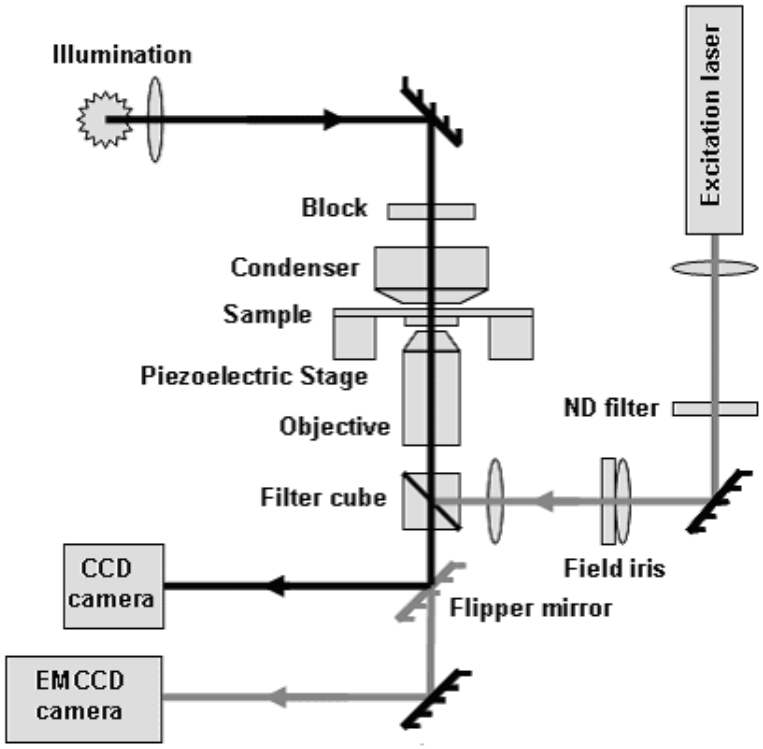

Figure 3.5: Important components in our fluorescent bead detection system. Fluorescence paths are shown in gray with light paths in black. The function of the components are described in the text.

Position detection

The position of a fluorescent bead in a frame was calculated by an iterative Gaussian mask algorithm. The centroid of the image was used as the initial guess. The mask was iterated until subsequent applications were within 0.05 pixels (2 nm) or 10 iterations were reached. The algorithm usually converged within 5 iterations.

More accurate fitting could be realised by application of a fully parameterised Gaussian fitting procedure but this was not necessary and considerably slowed data analysis. The Gaussian mask algorithm, as applied to simulated experimental data, demonstrated that the fitting procedure was not a limiting factor in accuracy (Chapter 5).

Calibration

The fluorescent detection was calibrated in a similar manner to the back focal plane detection system. The piezo stage was moved in a 0.1 μm radius circle (typical for the smaller fluorescent beads) and the 0.2 μm diameter fluorescent bead positions were measured. The calibration is shown in Figure 3.4. This system does not have any of the non-linearity present in the back-focal-plane system. The bead position is directly proportional to the centre of the detected spot and also does not depend on z-position. The calibration

constant was 44 ± 4 nm per pixel. The positional resolution of this method (∼5 nm) is discussed in Chapter 5.

3.2.5 The viscous drag on a bead

Torque was estimated by calculating the viscous drag on the bead, neglecting the contribution of the filament stub. An eccentrically rotating bead has a drag coefficient, $f = 8\nu r_b^3 + 6\nu r_b r_e^2$, where ν is viscosity, r_b is bead radius and r_e is eccentricity (Sowa et al., 2003). An average eccentricity of 0.20 ± 0.03 μm was measured using data from well aligned beads, giving f =20 ± 2 pN·nm Hz^{-1} for the 1 μm beads used. The estimated error of 10 % in f is from a combination of uncertainties in temperature (and therefore viscosity), bead radius and eccentricity.

3.3 Angle and speed measurements

3.3.1 Angle measurements

The three detection methods described above each produce data corresponding to the x- and y-position of the bead or cell. In the case of tethered cells it is possible to extract an orientation directly from the images but it proves to be more robust to consider the centre of mass of the cell as it describes

a circular orbit thus producing similar data to bead detection and removing the ambiguity between orientations that differ by π radians.

To extract accurate angle data it is necessary to introduce the assumption that the bead (or centre of mass of the cell body) describes a circular orbit around the motor axis. For a bead spinning on the motor of an immobilised cell this orbit is unlikely to be orthogonal to the optical axis of the microscope. Instead the orbit is tilted and observed as an ellipse, the major axis of which is the radius of the circular orbit.

Data are centered and can be ellipse corrected to give a circular orbit around (0, 0). The angle is then calculated from the argument of the complex number $z = x + iy$. In the case of long measurements where there may be some drift in the position, size and shape of the orbit, the centralisation is usually calculated over a moving window incorporating several seconds of data either side of the data point. Ellipse correction is more computationally intensive therefore data is usually dealt with in short sections with a single calculation for each. Ellipse correction is not required when calculating speed per rotation (Section 3.3.2).

3.3.2 Speed measurements

Speed per rotation

Initial experiments with the flagellar motor used the time taken for a full rotation of a tethered cell to measure the speed (Block and Berg, 1984; Blair and Berg, 1988). The equivalent method, with either tethered cells or rotating beads, is to calculate speeds from the angle measurements that constitute a full, or nearly full rotation.

The first step is to define where to divide the rotations. In the case of an elliptical orbit it is desirable to define this angle at the flattest (fastest) point. Figure 3.6 shows data for an elliptical orbit (a) divided into rotations by angle (b). The speed is then calculated by the change in angle during this rotation ($\Delta\theta \leq 2\pi$) divided by the time (Δt) between first and last points.

Problems with this analysis method occur when the motor does not rotate smoothly. If there is a pause (c) this is usually registered as a lower speed although the data can often be discarded with a threshold on the mean square error to a straight line fit. If a switch occurs during a rotation (d) then the section of data can be discarded with a threshold on $\Delta\theta$. With noisy slow rotation (e) it is difficult to define the start and end of a single rotation. Smoothed data can be used for division into rotations which are then imposed back on the unsmoothed data.

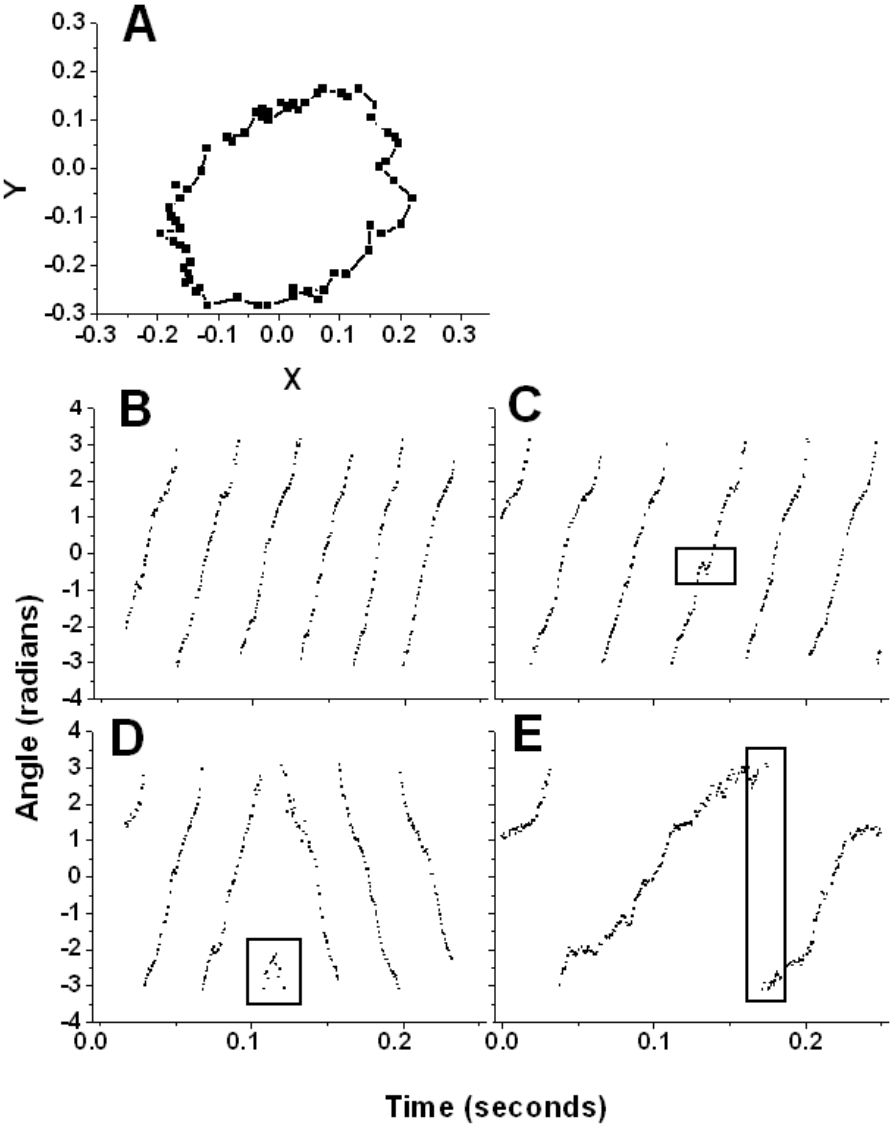

Figure 3.6: Difficulties encountered when measuring speed per rotation. In this case bead x-y data (a) is converted to angle (b) from which the speed can then be calculated. Problems encountered, highlighted by boxes, include pausing (c), switching (d) and noise in slow rotation (e).

Power spectrum analysis

The power spectrum analysis extracts speeds directly from the x-y data. The Fourier transform of a section of data gives a power spectrum, the peak of which is the dominant speed of oscillation in that section. This method has the advantage that circular orbits are not required and sensible results can be obtained from any signal that is periodic and representative of the motor rotation. Windows of 1 s are required (typically 2000 data points) in order to give 1 Hz speed resolution. To give time domain information a moving window approach is applied with the window weighted towards the centre.

The choice of window and weighting towards the centre has implications for the detection of short events. The detailed application of weighted windows and their effects on event detection are beyond the scope of this thesis but we should be aware of the possible problems that may arise. In order to obtain maximum time resolution we would like to apply as narrow a weighting as possible. However, the narrower the weighting, the broader the peak in the power spectrum and the more difficult it is to distinguish changes in speed. Another artifact is that an instantaneous speed change can look like a smooth transition. Our weighted window must also be wide enough to allow an accurate estimate of the periodicity at the slowest speeds expected. In practice we use a "flat top" window built from four cosine coefficients with a

full width at half maximum of 0.2 s. This is sufficient to accurately measure rotation down to about 3 Hz. Events shorter than ~ 0.1 s are missed by this analysis.

An example of the x- and y-signals, weighted by the flat top window, is shown in Figure 3.7. The power spectrum obtained from the Fourier transform of this data is shown alongside with the peak being the measured speed.

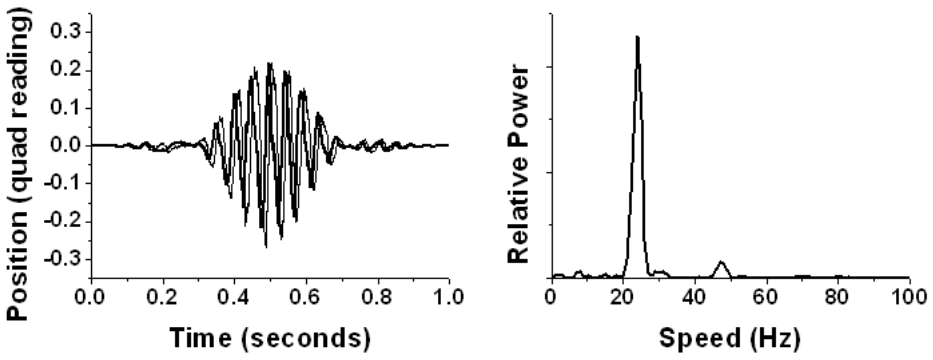

Figure 3.7: Quadrant photodiode x-y data weighted by the flat top window (left) with power spectrum (right). The window improves time resolution allowing shorter events to be observed. The calculated speed is the peak of the power spectrum.

3.4 Event detection

Separating real events from noise in biological data is a long standing challenge. What is thought of as noise is often not due to the experimental systems or any background readings but is due to biological processes that

we may or may not understand. Our analysis method must be tailored to each experiment in order to pick out the events under investigation as reliably (and automatically) as possible. The types of events we are interested in here are abrupt changes in speed or angle, steps, that help us to understand the mechanism of the motor.

Section 3.3.2 described a method of extracting the motor speed from position measurements based upon a moving window power spectrum. This is the method used in the bulk of experimental results in Chapter 4 and is well suited to detecting events happening on the tens of seconds to minutes timescale, removing much of the "noise" associated with more rapid speed change events. However a significant amount of noise remains, including pauses and switches in the case of speed measurements, and must be carefully dealt with.

3.4.1 Filtering

The events we are interested in are abrupt changes in speed therefore any mean averaging filter is not going to be appropriate as it will tend to soften hard edges. Two filtering methods produce sensible results as shown in Figure 3.8. The first is a median averaging filter. This preserves any step edges in the data whilst reducing the noise on individual speed levels. The second filter

is based on the method of Chung and Kennedy (Chung and Kennedy, 1991). Consecutive windows are passed through the data. The filtered value at the junction of the two windows is effectively the mean of the window with the lowest variance. This produces a mean averaging filter effect but conserves any step edges present as the window containing the step will have a higher variance than the other. Both these filters produce reasonable results to the eye however the step analysis methods developed were more robust with unfiltered data.

3.4.2 Stepfinding

Two methods were explored to find steps in the speed data. Both methods utilise the Student's t-test as a measure of step quality. Both methods were competent at finding the steps but the first method, steps by elimination, reproduced the original data from the found steps more accurately and was therefore also more accurate in determining the speed levels between steps. Both step finding methods are described in the following paragraphs. Calibration and application of the stepfinder by elimination is described in further detail. Application of the two stepfinder methods to an example data trace is shown in Figure 3.9. The parameters used were those determined in the calibrations (Section 3.4.2) for steps by elimination and a set that detected

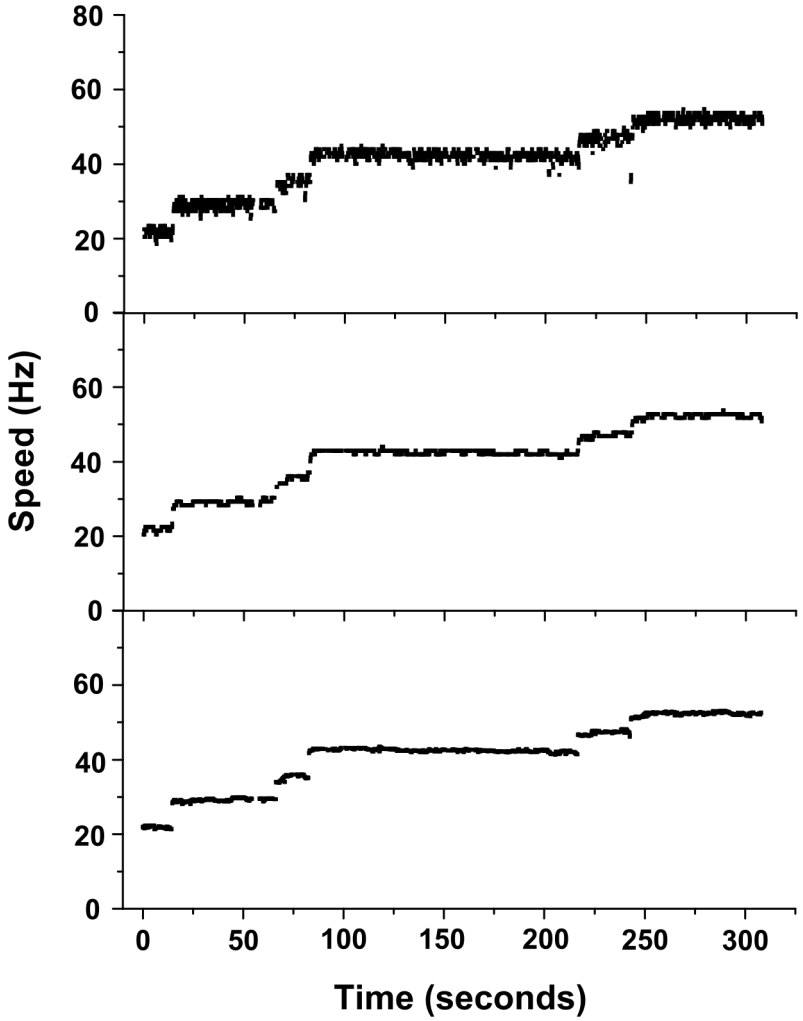

Figure 3.8: The application of filters to a passage of resurrection data. Both the median filter (middle) and the Chung-Kennedy filter (bottom) produce a reduction in noise to the eye. However for subsequent analyses the raw data trace (top) was used.

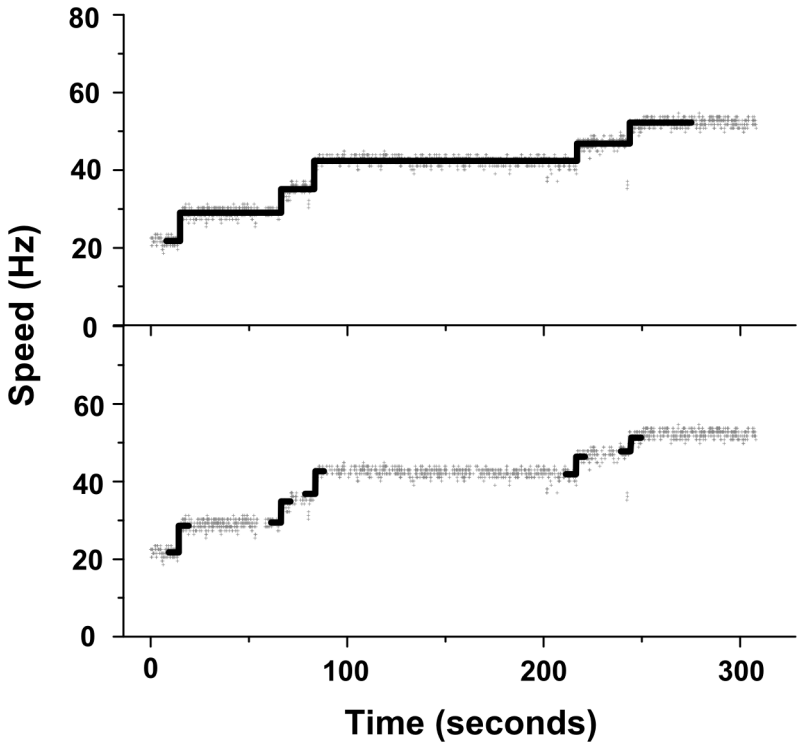

Figure 3.9: Comparison of the two stepfinding methods. Steps by elimination (top) allows for complete reconstruction of the idealised experimental trace. The running difference method (bottom) produces a disparity between the found step sizes and the levels in between.

the same steps for running difference (5 s window, threshold 10).

Steps by elimination This method is based on an idea (Kerssemakers et al., 2006) where the best steps in a dataset can be found by assigning a step at the position that minimises the error to a fit step function. The data is then divided at that point and the method reapplied on either side of the step. This method proved unreliable in detecting all the steps and often found steps in the noise. However it was a useful tool in generating a set of

steps that contained all the "true" steps as used in the following procedure.

1. The entire speed time trace was divided into two intervals at the point that gave the best least-squares fit to a single step function.

2. This process was repeated for each interval until either the best position was at one end of the interval or the interval was less than three data points. This produced an excess of steps within which all the "true" steps were contained.

3. A Student t-statistic was generated by comparing intervals immediately before and after each putative step (Leake et al., 2004).

4. The step with the lowest t-value was discarded and the surrounding intervals concatenated.

5. Step 4 was repeated until all remaining steps had a t-value above a set threshold. The threshold was determined by testing the algorithm on simulated traces containing Poisson distributed steps, with size, number, interval between steps and noise level similar to experimental traces.

Steps by running difference The running difference method detects steps by peaks in the running difference between the means of two consecutive windows as they pass through the data. A t-statistic is calculated for

each peak value, based on the windows either side, and steps can be identified where the t-statistic is above a given threshold. This method detects steps with a quantifiable sensitivity and specificity, unlike the elimination method where thresholds are set by simulation. The method does not accurately reproduce the levels between detected steps since it considers only the data within the windows rather than the whole level.

Resurrection steps

Preliminary inspection of experimental data shows that resurrection steps take place on a timescale of tens of seconds to minutes. There are both upwards and downwards steps present although downwards steps are much less frequent. For a 1 μm bead, steps are between 5 and 10 Hz up to a maximum of 80 Hz. Noise is present on each speed level with magnitude approximately $\pm$ 3 Hz and does not have any obvious dependence on speed. Switches are present in some of the data but these are removed in pre-processing.

In order to calibrate the stepfinder we create a simulated dataset of twenty resurrection traces. A resurrection trace is modeled as a Poisson stepper, magnitude 5 Hz, with upwards and downwards rates set so that a speed of approximately 70 Hz is obtained after 10000 data points (equivalent to about 17 minutes in an experimental trace) with occasional downwards steps. Gaussian white noise with a standard deviation of 3 Hz is superimposed upon

the Poisson trace to produce data qualitatively similar in both amplitude and power spectrum to experimental data. The simulated dataset consisted of 20 traces with a total of 292 steps.

Figure 3.10 shows the calibration of the threshold with a simulated dataset. A t-threshold of between 10 and 30 was explored delivering an excess and a shortfall of steps respectively. A real detected step in the simulated data is defined as 5 ± 1 Hz, -5 ± 1 Hz or 10 ± 1 Hz. These represent an upwards step, a downwards step and a double upwards step. The double upwards step was required to account for the Poisson stepper taking two steps in rapid succession, much more common than the reverse since downwards steps were rare. Specificity, a measure of the number of erroneous steps ($1 - \frac{true\ steps\ found}{total\ steps\ found}$), is greater than 90 % between T = 15 and T = 22 while sensitivity, the ability to detect the true steps ($\frac{true\ steps\ found}{total\ simulated\ steps}$), begins to fall off after T = 20. We also see that the number of steps detected between ± 3 Hz (steps in the noise) falls to zero at T = 20. We therefore choose T = 20 as our threshold for detecting resurrection steps.

The stepfinder as applied to a real piece of data with this threshold was shown in Figure 3.9. This figure illustrates the accurate reconstruction of the original data from the found steps. The stepfinder is applied to a large dataset in Chapter 4.

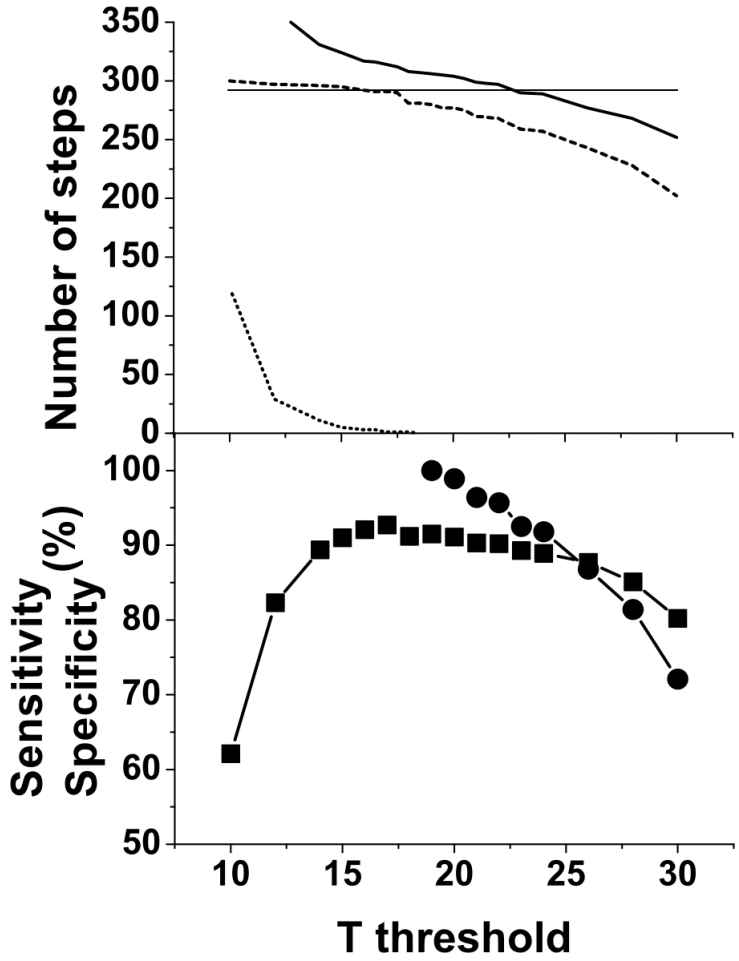

Figure 3.10: Calibration of the stepfinder. The number of steps in the dataset (292) is shown (top, thin line). The total number of found steps (thick line) decreases as the threshold increases. The number of true steps found (dashed) and the number of steps in the noise (dotted) also decreases. The sensitivity (bottom, circles) decreases after the threshold passes 19 while the specificity peaks at about 17. T = 20 was chosen as the threshold for resurrection step detection.

Chapter 4

Controllable induction of torque-generating units

Three methods to control the number of torque generators in a motor are explored in this chapter. The first method uses low to full induction of a plasmid carrying the relevant genes during culture of the cells to produce a steady state number of units in each motor. These numbers can be varied between a single unit to a full (WT level) motor. The second method, resurrection, relies on high induction whilst under observation. In this manner the incorporation of units into previously empty or almost empty motors can be observed. The third method uses the WT strain with cells observed in

the early stages of motility.

These three methods allow comparisons to be made between low unit and full motors. Dependence of properties of the motor on the number of torque generators and the incorporation of these units are investigated.

An important part of the work contributing to this chapter is the development of a reliable assay for low induction motors containing 1-3 units. This assay will allow a number of experiments to be performed in the future to compare properties such as the torque speed curve of single units to full motors. The low unit assay is also useful to study rotational steps (Chapter 5).

All the experiments in this chapter were performed with 1 μm latex beads. In this regime the torque-speed curve is roughly flat (Section 2.4) such that if each unit delivers an equal increment of torque, the resultant speed increments should also be approximately equal.

The bulk of this work was published in Proceedings of the National Academy of Sciences USA (PNAS) in May 2006 (Reid et al., 2006).

4.1 Steady state induction of torque-generating units

The three strains lacking chromosomal torque generator genes, MotA, MotAB and Chimera were cultured with inducer present. A low level of inducer results in a variable number of torque generators within each cell. It is likely that these torque generators exist as fully formed complexes, $MotA_4MotB_2$, in the cell membrane finding the motors by a diffusive process. There is association and dissociation from the motors, between four and six per cell, resulting in a steady state number of torque generators at each motor.

A similar effect is produced in the WT strain where torque generators are under the natural regulation system. Cells are harvested early when there is a lower number of torque-generating units in each motor.

4.1.1 Data

MotA strain Figure 4.1a shows speed histograms for populations of the MotA strain under low induction (5 μM IPTG) and high induction (500 μM IPTG). Each cell was observed for 20.4 seconds during which interval the speed was calculated 194 times. Low induction gave rotational speeds grouped at discrete levels separated by roughly equal intervals. These low induction peaks represent motors with 1, 2 and 3 units. These peaks are fit

Strain	1 unit	2 units	3 units	Full
MotA	7.5 ± 1.4	15.1 ± 1.9	21.4 ± 1.7	61.7 ± 7.8
MotAB	7.1 ± 1.7	13.8 ± 1.7	20.3 ± 1.7	64.0 ± 6.9
Chimera	8.7 ± 1.0	16.1 ± 1.9	24.1 ± 2.4	91.8 ± 3.7
WT				61.6 ± 5.7

Table 4.1: Low and full induction speeds (Hz) by Gaussian fit to histogram peaks

by a multiple Gaussian distribution and results shown in Table 4.1.

Intermediate concentrations of inducer did not tend to produce motors with intermediate speeds around 40 to 50 Hz but instead produced a mixed population of lower induction and full induction. This is probably due to the on/off nature of the lac promoter (Kalir et al., 2001).

Full induction gave speeds grouped around 60 Hz that correspond to a full motor. Separated peaks were not observable at full induction.

MotAB strain Histograms and fit speeds for the MotAB strain are shown in Figure 4.1b and Table 4.1. These data are qualitatively similar to those of the MotA strain. Again we get discrete peaks at low induction and a broad peak for full induction. It is more difficult to obtain single unit motors with this strain although intermediate speeds were more accessible. This is most likely due to different properties of the ara promoter as opposed to the lac promoter. Another possibility for these differences is the genetic background,

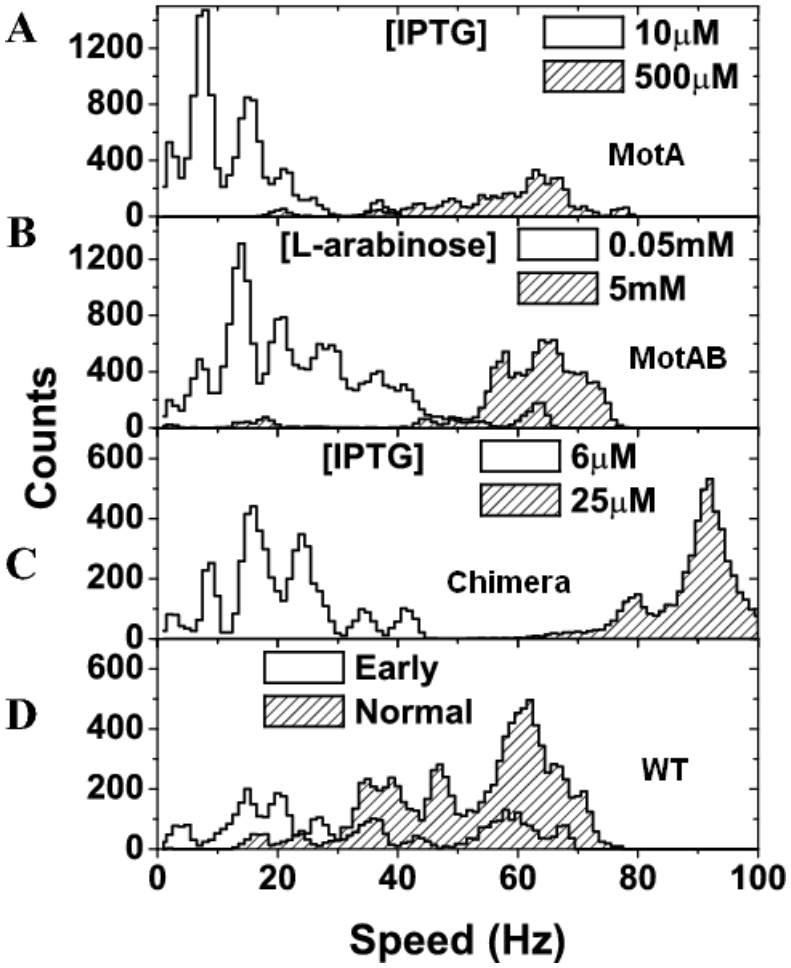

Figure 4.1: Steady state induction of stator proteins. (a) Speed histograms for MotA strain populations at low (10 μM IPTG, 40 cells) and high (500 μM IPTG, 26 cells) induction. (b) MotAB strain populations at low (0.05 mM L-arabinose, 107 cells) and high (5 mM L-arabinose, 52 cells) induction. (c) Chimera strain in 85 mM sodium chloride at low (6 μM ITPG, 30 cells) and high (25 μM IPTG, 30 cells) induction, data collected by CJL. (d) WT strain harvested early (2 hours, 24 cells) or at the normal time (4 hours, 52 cells). At low induction, peaks occur due to discrete numbers of torque-generating units. The width and distribution of peaks is discussed in Section 4.1.2.

here a deletion followed by induction of *motA* and *motB* compared to the point mutation background of the motA strain.

Chimera strain Since the Chimera strain is a sodium driven motor its results are not directly comparable with those of the proton-driven strains although at 85 mM sodium chloride Chimera displays similar trends. Low speed peaks are clearly observable as is the broad full induction peak. The full speed of Chimera under these conditions is higher than that expected based on the single unit speed indicating either a different number of units present or a different torque-speed characteristic. The purpose here is to show that the low induction peaks are similar in the sodium-driven motors and therefore a property of the flagellar motor in general rather than a property of our inducible proton-driven strains. Histograms and fit speeds are shown in Figure 4.1c[1] and Table 4.1.

WT Early harvesting of the WT strain shows cell speeds in groups that also correspond to low numbers of torque generators. The full speed of the WT shows a broad peak around 60 Hz corresponding to full induction in the other proton-driven strains. This is contrary to previous results (Blair and Berg, 1988) where the wild type speed was slower than that of a fully induced strain. The previous results were obtained with tethered cells where

[1]Data collected by CJL.

faster cells may have broken their tethers and viscous loads were variable. Our experiments show a peak at about 40 Hz, below the full speed peak. This might be interpreted as the top speed, were the full speed peak missing, explaining this discrepancy.

4.1.2 Results

The ability to resolve low induction peaks is a good indicator of the reproducibility of our spinning bead assay. Narrow peaks demonstrate similar viscous loads and therefore similar bead orbits. The peaks also show that inter-cell pmf variation is low and that day to day reproducibility of the assay (temperature, growth conditions etc.) is also good. Approximately half the width of these peaks can be attributed to fluctuations within the speed of an individual cell, the other half due to the factors discussed above. For example, the level 2 peak for the MotA strain is fitted as 15.1 ± 1.9 Hz (Figure 4.1a and Table 4.1). Of 14 cells that showed a steady level 2 (i.e. no level changes or pauses) the average standard deviation within each measurement was 1.3 Hz, attributed to speed fluctuations of each motor. The mean values for each measurement varied with a standard deviation of 1.1 Hz attributed to variations in protonmotive force and viscous drag coefficient. Adding these two contributions in quadrature gives 1.7 Hz, close to the observed peak width

of 1.9 Hz.

The range of speeds observed at full induction and in the WT strain may correspond to the variability in the torque produced by a single unit, which is reflected in the width of the low induction peaks, however this does not seem likely. Were this the case we would expect the width of the level 2 peaks to be twice that of the level 1 peaks and this trend is not observed. The speed range, particularly in WT where lower speeds are observed, is likely to be due to variability in the number of torque generators present in the motor.

Figure 4.2 shows the variation in mean speed for populations of cells, measured over two separate experiments, at a range of inducer concentrations. Mean speed saturates at approximately 60 Hz for both inducible strains, similar to the full speed observed in the WT strain. The error bars (standard deviation), greatest at intermediate concentrations, are due mainly to variation between individual cells, demonstrating variable sensitivity to induction within each population. At low induction, speeds are higher than expected since only spinning cells are measured (i.e there is a bias against 0 Hz cells). Immuno-blots for the presence of MotA were performed[2] with both MotA and MotAB strains. MotA strain results showed presence of MotA, as expected, with and without induction. MotAB strain results showed absence of MotA at zero and very low induction with increasing amounts present at

[2]Immunoblots were carried out by JC.

higher induction levels (Figure 4.2 inset).

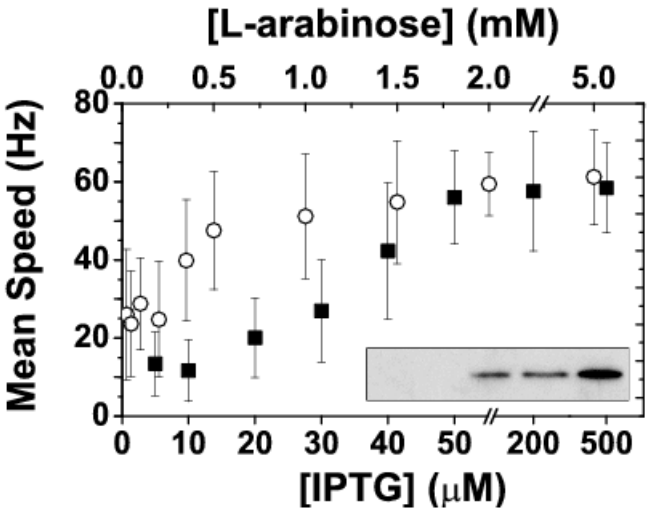

Figure 4.2: Mean motor speed in populations of cells at a range of inducer concentrations. Filled squares are MotA strain at a range of IPTG concentrations; open circles are MotAB strain at a range of arabinose concentrations. Each point is the average of at least 25 cells. Error bars are the standard deviation of each population. Inset: Immunoblot for MotAB strain showing an increase in the amount of MotA present at L-arabinose concentrations 0, 0.05, 0.25, 0.5 and 5 mM.

4.2 Resurrection

Experiments in which high concentrations of inducer were added while a single motor was under observation were performed on all three inducible strains. Cells were cultured with low-level induction (5 or 10 μM IPTG for the MotA strain, 10 μM L-arabinose for the MotAB strain and 6 μM IPTG

for the Chimera strain) so that motors with one or two units and well-aligned beads could be selected before further induction.

4.2.1 Data

MotA strain Figure 4.3a shows a typical resurrection from the MotA strain with analysis from the stepfinder superimposed. To the right is a speed histogram that illustrates the different levels clearly. In a dataset of 21 resurrections[3] speed increases began 10-20 minutes after addition of inducer (typically 1 mM IPTG) with maximum speeds reached after an additional 10-20 minutes. 16 of these experiments reached level 10 or above. The resurrection in the figure clearly shows levels 1-11 and possibly level 12.

Tethered cell resurrections were complicated by cell growth during observation (Figure 4.4). In order to get a cell to resurrect it was necessary to provide some nutrients to enable synthesis of new protein. Growth resulted in an increase of drag coefficient and therefore a slowdown in speed. Despite this more than eight levels can still be counted by eye.

MotAB strain A typical resurrection is shown in Figure 4.3b. In a set of eleven resurrections, eight reached level 10 or above with the resurrection shown clearly going from level 2-10. Speed increases began 20-30 minutes

[3]Three of these resurrections were collected by RB, three by ML, the remainder by myself.

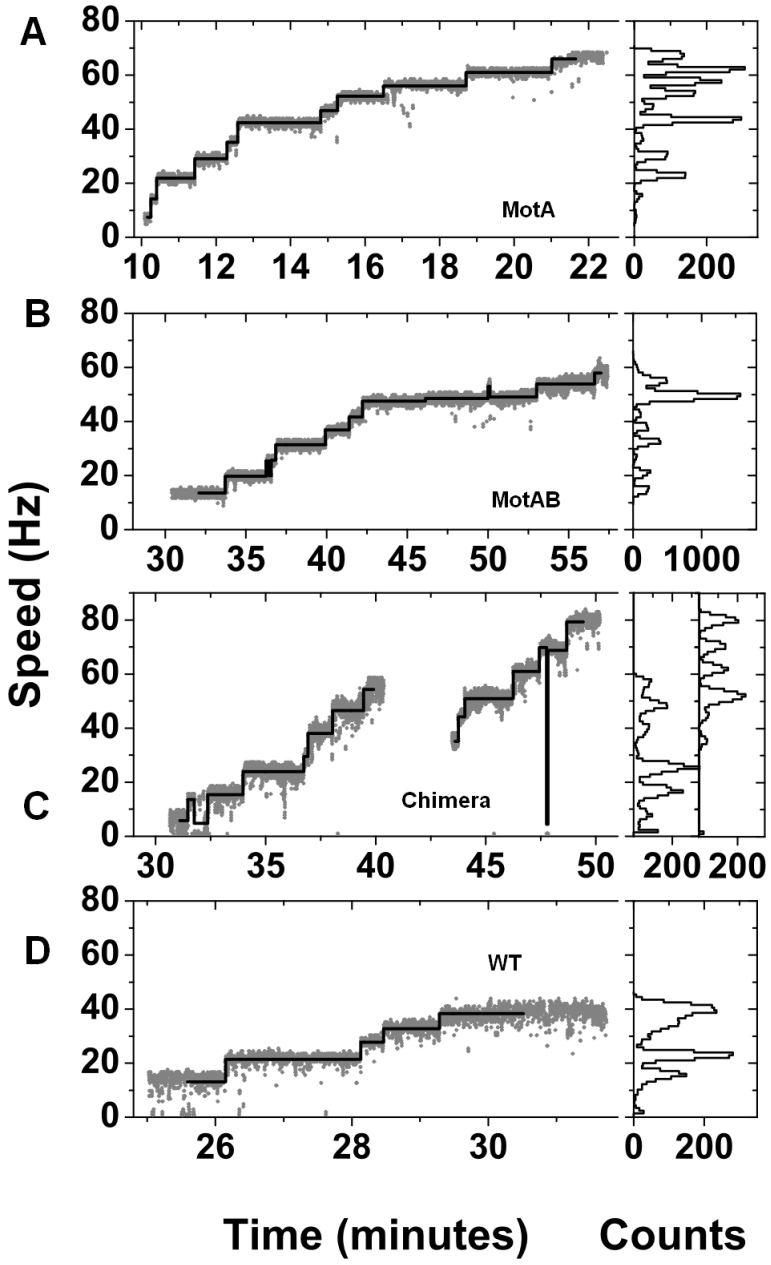

Figure 4.3: Resurrections for MotA, MotAB, Chimera and WT strains respectively. Levels found by the step-finder routine are superimposed and speed histograms are shown on the right. The MotA strain shows levels 1-11 (possibly 12); the MotAB strain shows levels 2-10; Chimera strain shows levels 1-7 and 5-10 (or perhaps 4-9) in two different cells recorded consecutively in the same preparation; the WT strain shows speed increments consistent with levels 2-6.

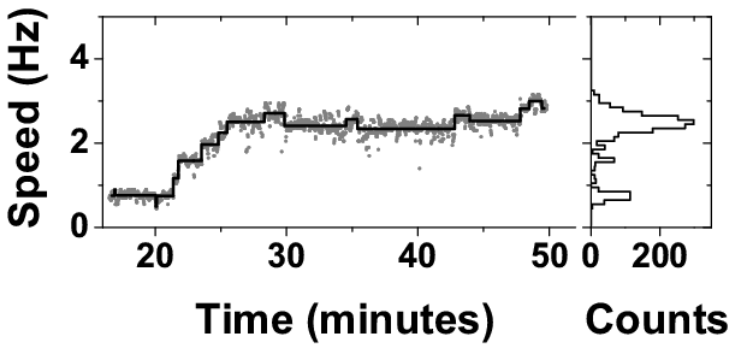

Figure 4.4: A tethered cell resurrection of MotA. Speed increments are clear between levels 2-8 with possibly level 10 reached by the end of the observation. The speed histogram (right) is less clear than for bead resurrections.

after addition of inducer (5 mM arabinose) with maximum speeds reached after an additional 30-60 minutes.

Chimera strain Full resurrection traces were much more difficult to obtain with the Chimera strain, an indicator that perhaps the Chimera stators are less stable than the those in the other strains. The data shown in Figure 4.3c is from two cells in the same preparation showing levels 1-7 and 5-10 (possibly 4-9)[4]. These data illustrate that resurrection is qualitatively similar in the chimeric sodium-driven motor to that of the proton-driven motors.

WT A novel approach produced a resurrection-like experiment using the WT strain, where expression of mot genes is under natural regulation from the chromosome. Cells were harvested early during growth (only two hours

[4]Data collected by CJL.

after inoculation, compared to the usual four) and observed in motility buffer supplemented with 5 % tryptone-broth (similar to resurrection buffer but without inducer). In population measurements, a broad range of speeds were observed, with speed tending to increase with time. Average speeds within a cell population measured at times 0-30 minutes, 30-60 minutes and greater than 60 minutes were 32 ± 20, 44 ± 16 and 51 ± 15 Hz respectively. Figure 4.3d shows a typical speed trace and histogram for an extended measurement of a cell under these conditions. Speed changes in the trace are consistent with the incorporation of torque generators from level 2-6. The timescale of incorporation is consistent with that seen in the inducible strains.

4.2.2 Results

Induction of the MotA strain was about three times quicker than that in the MotAB strain as illustrated by the example traces of Figure 4.3. While it is tempting to draw conclusions about the formation and incorporation of the torque-generating units this difference is most likely due to different induction properties or copy number of the plasmids carrying the *motA* or *motAB* genes. The previous work (Blair and Berg, 1988) had resurrections of both mutation and deletion strains proceeding much quicker than in our experiments.

Variations were made to the experimental conditions in order to assess the effect on resurrection. Concentration of inducer in the resurrection buffer was varied over the ranges 100 μM to 2.5 mM (IPTG, MotA strain) and 2 mM to 5 mM (L-arabinose, MotAB strain). Tryptone broth was added to the resurrection buffer at concentrations between 1 % and 30 %[5]. Cells were grown for between 3-5 hours, at temperatures between 28 ^{o}C and 32 ^{o}C, and from either pre-frozen aliquots or saturated overnight cultures. Inducer was flushed out of the flow cell after five minutes incubation. An alternative motility buffer was used, based on HEPES instead of potassium phosphate. A mild detergent (0.005 % Tween-20) was added. A resurrection buffer containing sodium chloride, lactate and methionine, as used in previous work (Blair and Berg, 1988) was also used.

Resurrections using lower inducer concentrations did not usually attain full speed, even up to 2 hours after induction. Any trends observed in this regime were complicated by variable sensitivity between cells (i.e. some cells attained higher speeds than others at the same inducer concentration). Cells did not increase in speed when no T-broth was present. No other significant differences in the time-course, unit numbers, or speed levels were seen with any of the variations.

[5]T-broth, growth condition, HEPES and detergent controls were carried out by ML.

4.2.3 Stepfinder analysis

A combined MotA and MotAB dataset consisting of 32 resurrections was investigated. Speed vs time traces were analysed with the step-finding algorithm. To remove the effect of cell-to-cell variations, speeds were normalised as follows. The majority of resurrection traces (23 out of 32) included a level with a speed between 18 and 23 Hz, identifiable as corresponding to 3 units. Only these traces were analysed. Normalized speed was defined for each trace as 3 x (actual speed) / (mean speed at level 3). The average of all level 3 speeds was 20.8 ± 1.3 Hz, corresponding to a normalization constant of 6.9 ± 0.4 Hz per stator unit, consistent with the values determined in steady-state low expression experiments (Table 4.1). Normalisation did not alter the general trends in the data as can be seen by comparing the histograms in Figures 4.5a and b.

Figures 4.5b and c show histograms of all normalized speeds, and of the normalized speeds of levels found by the step-finding algorithm respectively (in Figure 4.5c; level 1 is badly defined because cells spinning with one unit often paused, causing problems for the step finder, and because many resurrections began from level 2; the lack of scatter at level 3 is a consequence of using this level for normalization). Levels 1-5 are clearly identifiable in the pooled histograms of Figures 4.5b and c. Higher speed levels are not easily

distinguishable indicating that these levels varied from cell to cell. Figure 4.5d shows separate histograms of normalized step size for steps in which the normalized speed level after the step was less than 5.5 (upper) and greater than 5.5 (lower). Gaussian fits to the main peaks give average normalized step sizes of 0.90 ± 0.17 and 0.75 ± 0.20, corresponding to 6.2 ± 1.2 Hz and 5.2 ± 1.4 Hz for lower and higher speed levels respectively. Figures 4.6a, b show normalized step size against normalized speed level after the step for all upwards steps found in normalized traces. The variation in step size is discussed in Section 4.3.

4.3 Torque per unit

4.3.1 Torque per unit decreases with increasing unit number

Resurrection speed increments were found to decrease with speed despite the fact that a 1 μm bead should be well within the linear, almost flat region of the torque speed curve. The maximum decrease in step size due to increasing speed alone, based on the torque speed curve, is less than 5 % (illustrated in Figure 4.8, triangles) over the full speed range but our results show a decrease of ∼40 %. To rule out the possibility that this result is an

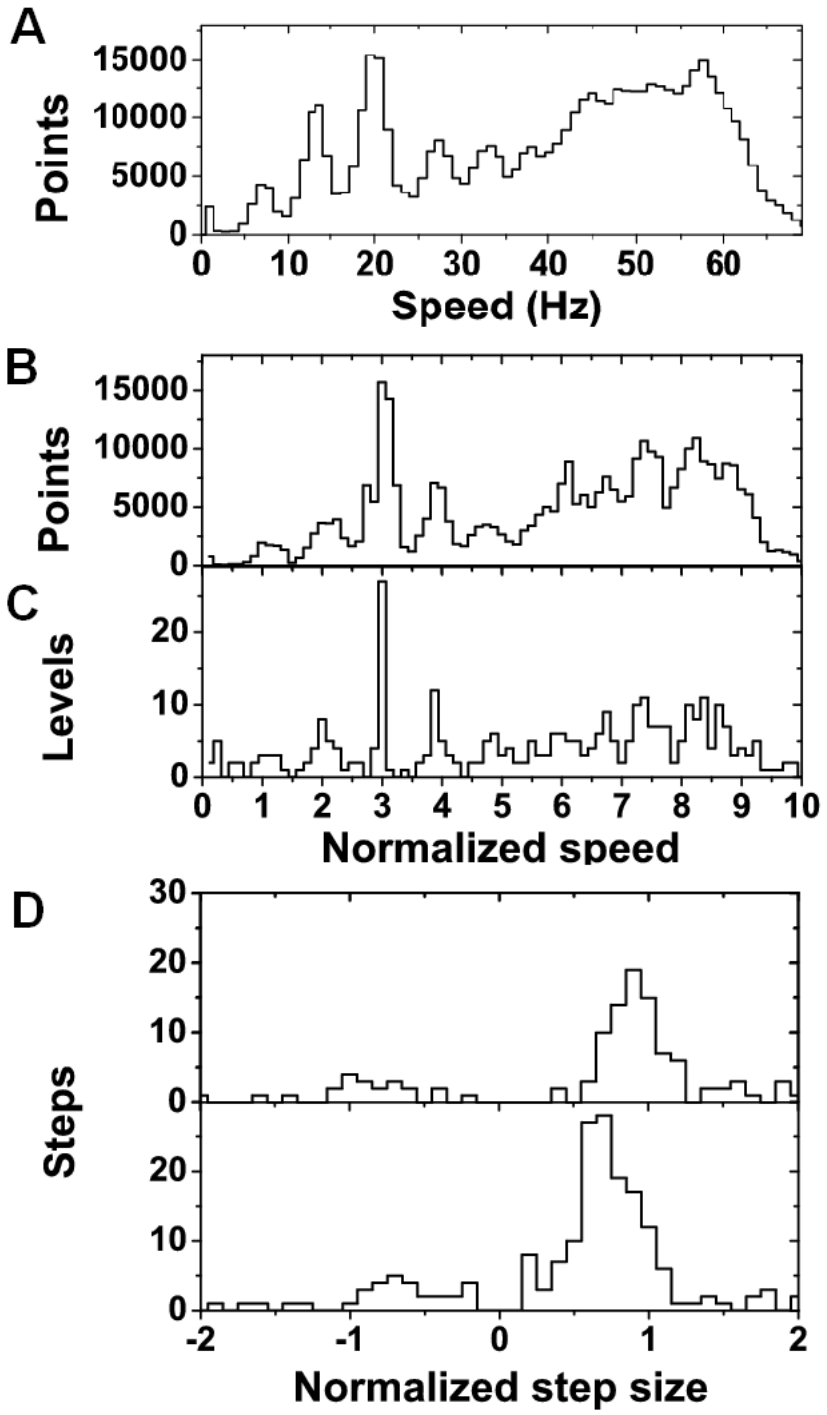

Figure 4.5: Results from the step-finder routine. Combined speed histogram from 32 resurrections is shown (a) above the histogram of combined speeds from the 23 normalised resurrections (b) and the histogram of found levels in those normalised resurrections (c). A histogram of found step sizes, split at 5.5 normalised units illustrates the decrease in step size at higher levels (d).

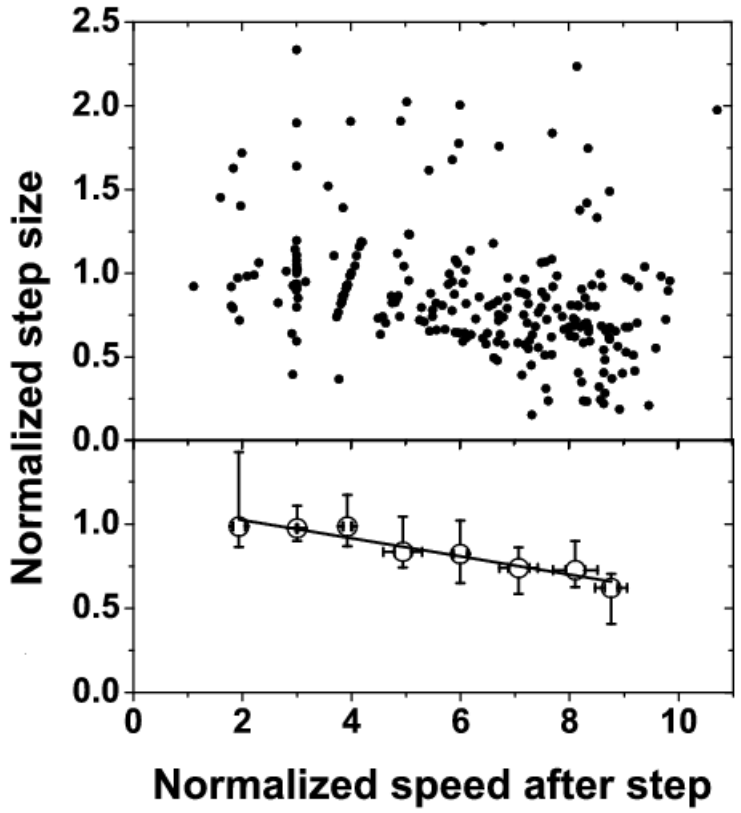

Figure 4.6: Step size during resurrection experiments. Normalised step size vs normalised speed for all upwards steps in 23 normalised resurrections (top). Median and interquartile range for the data, binned in 1 unit bins with a linear fit is shown (bottom).

artifact due to de-energization of cells expressing proteins in the low-nutrient motility buffer, we observed that resurrections in media containing lactate and methionine, used in previous experiments to prevent de-energization (Chen and Berg, 2000; Blair and Berg, 1988), also showed smaller step sizes at higher levels. Further evidence against de-energization as the cause of reduced step sizes came from extended observations of WT cells and cells grown with high levels of inducers, which showed speed steps smaller than one eighth of the speeds either side of the step consistent with more than 8 units and a reduced step size at higher levels. An example of steps in a full speed cell is shown in Figure 4.7 along with the histogram of found step sizes for 17 (5 WT, 5 MotA, 7 MotAB) measurements totaling 294 minutes. The speeds at the end of resurrection traces were similar to those of WT cells and those fully induced during growth providing further evidence. Bead orbits did not change significantly in size or shape during resurrection ruling out a change in viscous load as an alternative explanation of the reduction in step size.

The reduction in step sizes at higher levels indicates an interaction between torque-generating units that reduces the torque delivered at high numbers of units. Interactions may be via the rotor, directly due to close packing of stator units, or due to some other unknown mechanism. Due to experimental difficulties, the Chimera strain resurrection dataset is smaller and less

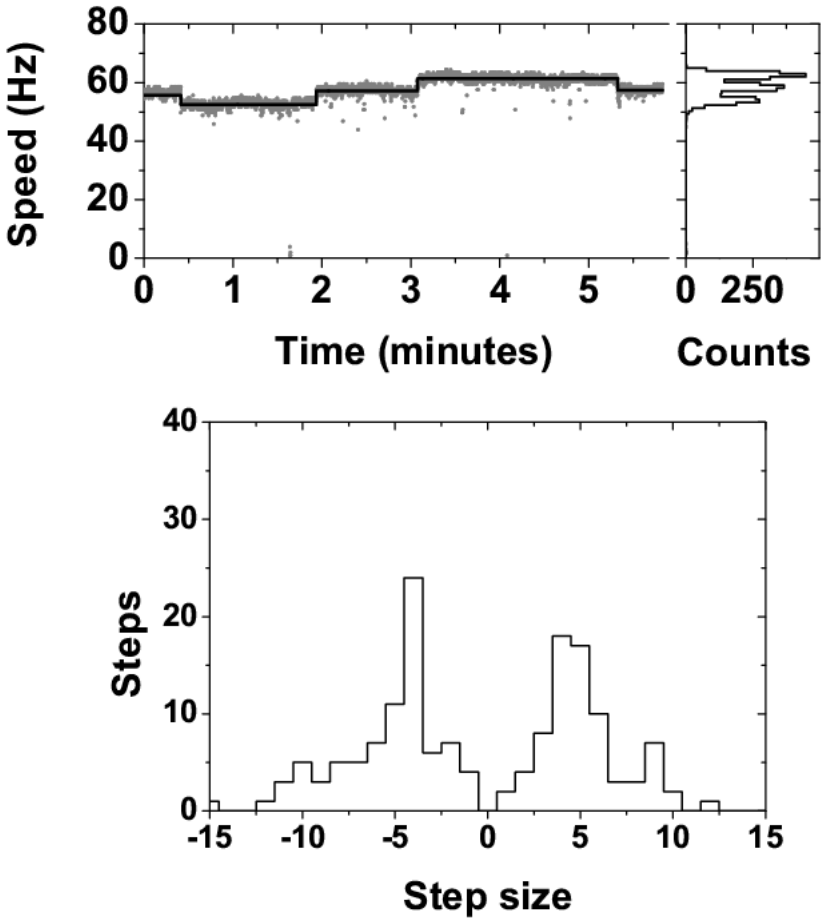

Figure 4.7: Steps in fully induced MotA, MotAB and WT cells. Steps found in a MotA strain trace are shown (top) with a histogram of steps from 17 traces of the three strains (bottom). The step size is consistent with those at the end of resurrection traces.

complete than the others, and an extended step-size analysis was not possible. However, the Chimera strain does not appear to show the reduction in step sizes at higher levels. This can be seen by comparing Figure 4.1c to Figures 4.1a, b and Figure 4.3c to Figures 4.3a, b. A possible explanation for this difference could be local proton depletion (speculation by David Blair) being responsible for the reduction in torque, not present in sodium-driven strains.

4.3.2 Torque estimates

The torque generated by a single unit rotating a 1 μm bead at 7.3 $\pm$ 1.6 Hz is estimated at 146 $\pm$ 35 pN·nm, and by a fully induced motor at 63 $\pm$ 7 Hz to be 1260 $\pm$ 190 pN·nm. The torque delivered by each unit in a fully induced motor is 121 $\pm$ 24 pN·nm using our estimate of unit number from Section 4.4. This is lower than the single unit torque due to the decrease in speed increment in full motors.

The single-unit torque is considerably lower than the value reported earlier using the same MotA strain (Ryu et al., 2000). Viscous drag on long filament stubs ($\sim$ 1-2 μm), ignored in our analysis, could possibly account for this difference. However, flagella were sheared in the same way in both experiments, and the lack of beads rotating at eccentricities greater than $\sim$

0.5 μm and the small variation in speeds from cell to cell are both evidence against long flagellar stubs. Fully-induced torque estimates are at the lower end of the range of previous measurements (Blair and Berg, 1988).

4.3.3 Energy balance

Assuming a proton-motive force (pmf) of -150 mV (Gabel and Berg, 2003), we can estimate a lower limit of 38 $\pm$ 11 for the number of protons that flow through each unit per revolution (equal to the work done by a single-unit motor in one rotation, $2\pi \times$ Torque = 917 $\pm$ 220 x 10^{-21} J, divided by the free energy per proton, -e $\times$ pmf = 24 $\times$ 10^{-21} J). Given the recent observation of 26 discrete angular steps per rotation of the motor (Sowa et al., 2005), the above estimate is consistent with the hypothesis that the fundamental torque-generating process in the flagellar motor uses more than one ion (Berry and Berg, 1999), but does not absolutely rule out the possibility of a single-ion step. Torque in the chimeric motor in 85 mM sodium was 20 % higher, perhaps indicating that the sodium-motive force (smf) is greater than the pmf under these conditions. Direct measurements of the smf at different sodium concentrations in cells with chimeric motors (Lo et al., 2006) may resolve this question in the near future.

4.4 The number of torque-generating units

The most conservative estimate of the number of torque-generating units in a maximally occupied motor, ignoring any effect of reduced torque per unit at high levels (Section 4.3), is obtained from steady-state induction data by dividing the typical speed of a fully induced motor by the average speed per unit at low levels. The former can be estimated as 63 ± 7 Hz by fitting the largest high induction peaks in Figure 4.1. Similar estimates of the fully-induced speed can be obtained from the highest speeds obtained in resurrection experiments. The latter is estimated as 7.2 ± 0.3 Hz, an average based on the data in Table 4.1 for MotA and MotAB strains at levels 1, 2 and 3, giving an estimate of 8.8 ± 1.0 units. More accurate estimates taking account of the observed reduction of torque per unit at high levels can also be obtained from resurrection data. Using the linear fit of Figure 4.6 and the average normalization constant to estimate the speed per unit, gives 10.4 ± 1.3 units in a typical fully induced motor. These estimates are illustrated in Figure 4.8 (squares and stars respectively). We can count up to 11 distinct speed levels in some cases, indicating that the higher estimates above are more accurate than the lower. Our estimate of at least 11 units in a maximally occupied motor is consistent with the number of intra-membrane particles (10 to 12) found by freeze fracture studies (Khan et al., 1988).

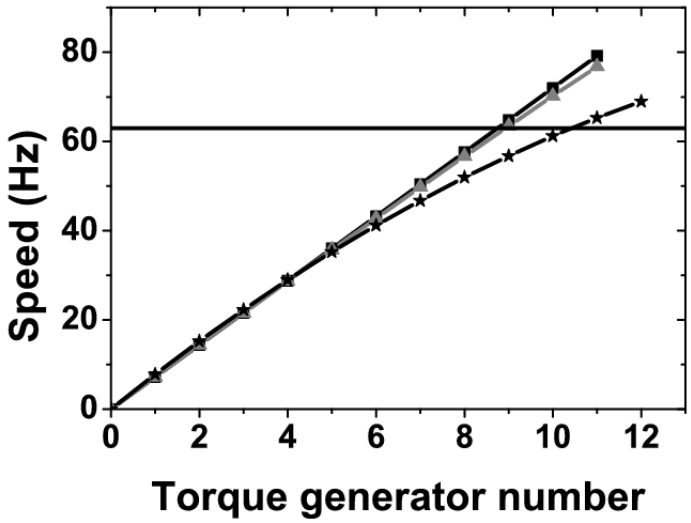

Figure 4.8: Models for speed vs. torque generator number. Squares, each unit contributes 7.2 Hz; triangles, the average unit torque decreases according to the measured torque-speed curve (Chen and Berg, 2000); stars, step size depends on speed as illustrated in Figure 4.6. The line at 63 Hz marks the average speed for fully induced cells.

4.5 Incorporation of torque-generating units

4.5.1 Resurrection Steps

Under resurrection conditions the number of upwards speed steps is greater than the number downwards resulting in the overall increase in speed from one unit to about eleven. In the steady state, the number of upwards and downwards steps is equal resulting in no speed change on average. No clear trends emerge when looking at the duration of intermediate levels during a resurrection. We can infer some properties of the incorporation of units into the motor by looking at the steps during resurrections in our dataset. At low

speeds there are approximately equal numbers of up and down steps due to cells starting at level 1 or 2 and pausing. There are few downwards steps until speeds reach about 50 Hz (level ~ 7) perhaps indicating that the arrangement of torque generators is least stable at this point. One possible explanation is that the motor has begun to fill up and that torque generators need to rearrange themselves in order to make room. This effect may also contribute to the difficulty in obtaining steady state motors with intermediate speeds (Section 4.1).

4.5.2 Brief detachments

There appears to be a process occurring on a faster timescale than the resurrection steps where the speed decreases by an amount attributable to either one or two units before recovering. These events are at the limit of the time resolution used for step detection. It is possible that these are due to units releasing then reattaching rather than resurrection steps which are units coming and going. Detachments happen more frequently than resurrection steps so it is unlikely that they are due to the same process.

These events are present both in resurrection and steady state low induction. Figure 4.9 illustrates the processes on both timescales. Resurrection steps are observed from levels 2-1-2-3 with brief detachments from 2-1, 3-

2 and 3-1. These detachments are also present in WT data but are more difficult to identify due to the smaller step size at high speeds.

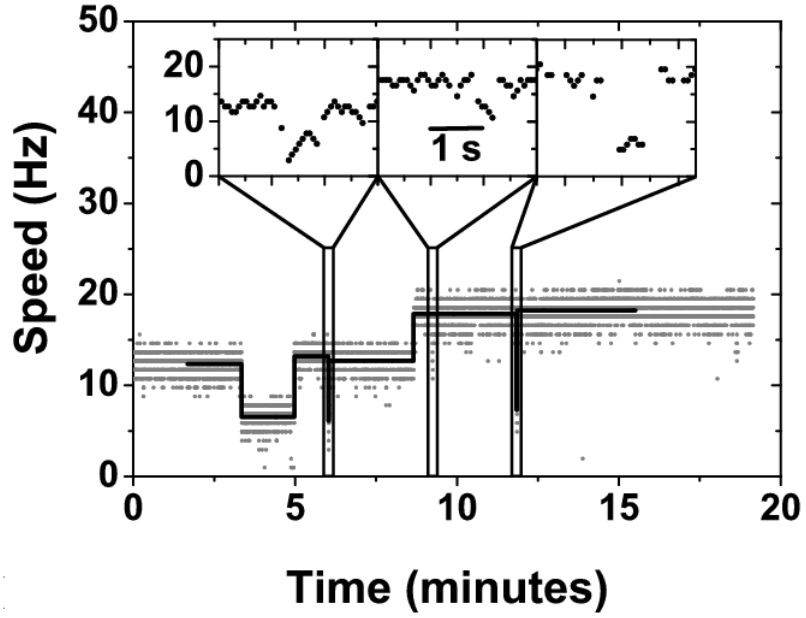

Figure 4.9: Speed changes during extended observation of a MotA strain cell at low (20 μM IPTG) induction. Resurrection speed increments are observed with brief detachments expanded in the insets. Levels found by the stepfinder are superimposed.

4.6 Switching and torque generators

The MotA strain is WT for chemotaxis which means that the motor switches. For resurrection analysis any CW speeds were removed and the data concatenated (although time domain information was kept). The simplest measure of switching is the CCW bias of the motor, the proportion of time spent in the

smooth swimming direction. It is suggested that the motor may sense proton flux (Fahrner et al., 2003) and alter its switching behaviour. It is likely therefore that the switching will be dependent on the number of torque generating units.

Figure 4.10a shows the CCW bias for 127 MotA cells at various inducer concentrations. The mean bias in each speed bin shows bias decreasing from 1 in single unit motors to about 0.9 at full speed. However even at full speed there are motors that did not switch at all. Figure 4.10b shows the bias from 12 MotA resurrections[6]. Each data point represents twenty seconds of data (comparable with a point in Figure 4.10a). The mean bias decreases in a similar fashion to the steady state motors. Here there is switching in single unit motors. Inspection of the raw data shows that single unit switching was only observed in 2 of our resurrections. More detailed studies of switching are currently underway in our lab.

At the sample rate used (2000 Hz) switches were instantaneous when investigated in the angle domain. However CW intervals less than half a second in duration were not detected with the power spectrum method. It is difficult to draw conclusions about how switching depends on the number of torque generators since we do not know how the chemotaxis network is

[6]Measures of bias required the plane of the bead orbit to be fairly flat such that the direction of the motor was well defined. Only 12 from 21 fitted this criteria. Those excluded were usually tilted side on to observation.

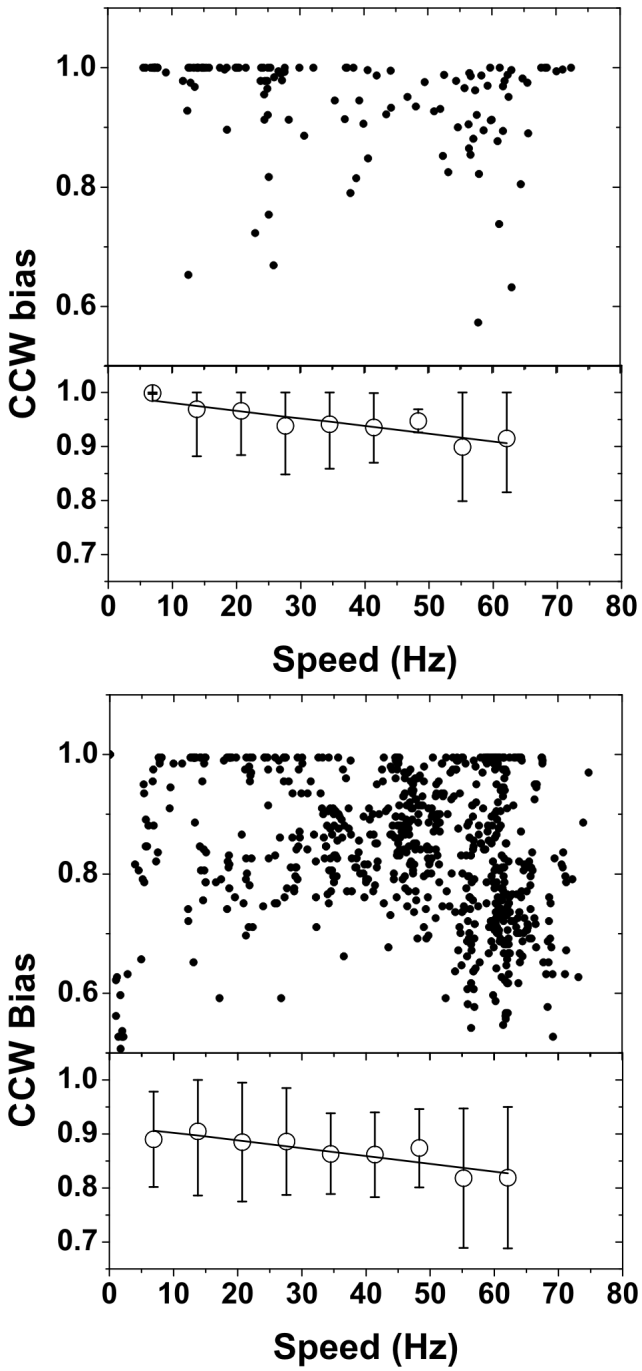

Figure 4.10: Counter clockwise bias at different speeds. The bias in steady state measurements (top) is measured over 20.4 s for 197 cells of the MotA strain. Twelve resurrection traces of the MotA strain (bottom) are split into 20 s intervals and the bias calculated for each. The mean speeds for each measurement are binned into 6.9 Hz bins (1 normalised unit for resurrection traces). The mean bias for each bin is plotted below illustrating the decreasing trends. Linear fits are shown and error bars are the standard deviation within each bin. The maximum bias is 1.

responding to our experimental conditions. For example the bias of 0.9 in resurrecting cells at one unit compared to a bias of 1 in steady state is possibly due a chemotactic response to the induction of the plasmid.

Chapter 5

Rotational steps

Measurement of rotational steps, i.e. non-smooth rotation of the motor, gives information about the detailed function of the motor. A periodicity of 26 steps per rotation was observed in motors slowed down by either cumulative photodamage or sodium de-energisation (Sowa et al., 2005). This was the first observation of stepping in an ion-driven motor and concluded that the periodicity observed was consistent with that of the FliG protein in the rotor. Backwards steps were also observed indicating that the free energy change per step was small, similar to that of a single ion transit. It was not possible to draw more detailed conclusions since the stepping was only observed with motors in a transient "near death" state. The development of a stable assay

for slow rotation, coupled with high speed, accurate position detection is an important follow up to the initial observation of stepping.

This chapter reproduces the initial observation of stepping in the Chimera strain and details progress towards an assay based on fluorescent bead detection that addresses the issue of fluorescence damage. A fluorescent bead assay is preferable to a back focal plane detection system since smaller beads can be used, reducing the load on the motor and the relaxation time of the elastic hook linkage (from $\sim$ 1 ms to $\sim$ 0.15 ms (Block et al., 1989)), and the bead detection method is linear. Reduction of the motor speed to allow stable observation with resolved steps is also discussed.

5.1 Fluorescence damage

Fluorescent photodamage is the main limitation to be overcome. The exact mechanism of damage to motors is not known however the damage is a local effect perhaps due to photoactivated reactive oxygen species being released by the fluorescent bead whilst under observation. Experimental observations support this hypothesis. Fluorescent beads on long tethers (several microns rather than tenths of microns) do not slow down as much under fluorescent observation but are not useful to measure the steps. Latex beads of the same size do not slow down when illuminated with similar laser powers as those

used for detection and tethered cells take several minutes to stop rotating when illuminated with laser powers ten times more intense.

Figure 5.1 shows a typical speed time trace for the yellow/green bead assay as used previously (Sowa et al., 2005). The strain was Chimera with full induction. Beads were 200 nm diameter. Images were recorded at 2.4 kHz with bead brightness $\sim$ 10000 counts on the EMCCD. Images were analysed as described in Chapter 3. There were several minor differences to the previous work. An argon ion laser was used for more efficient excitation rather than a mercury arc lamp. The apparatus was also different, custom built for fluorescent observation rather than combined with the back focal plane apparatus. Photodamage occurred on a similar timescale to that previously observed. This cell is one of the longer lived with most others stopping quicker, within a couple of seconds. Stepping data can be obtained from the boxed "near death" region around 6 seconds.

Three methods were explored to reduce the photodamage to a point where observations could be made with cells rotating steadily. Longer wavelength (crimson) fluorescent beads were used rather than the shorter wavelength yellow/green beads. Also the laser power was reduced to the minimum possible for accurate observation. Finally a substrate to mop up reactive oxygen species was added.

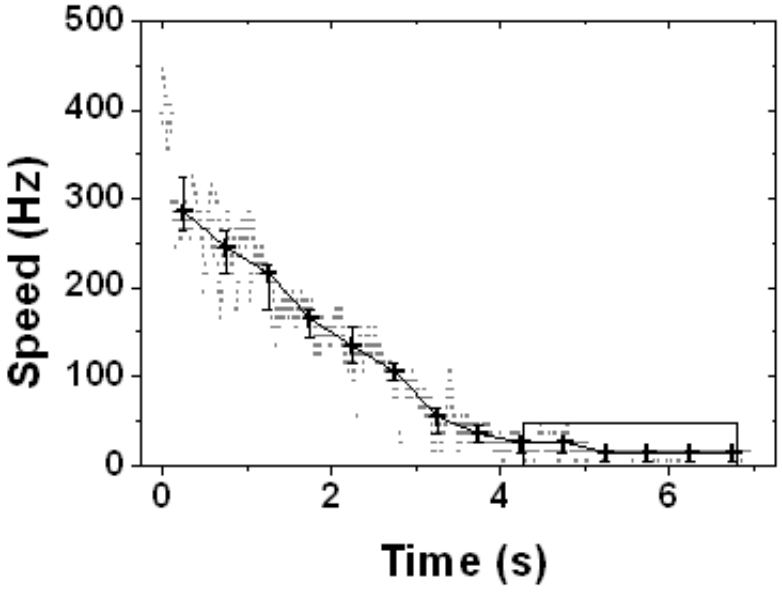

Figure 5.1: Fluorescent photodamage during an experiment under conditions similar to the previous work (Sowa et al., 2005). The boxed region shows where stepping data can be obtained. Median speeds are superimposed with interquartile range error bars. Speeds appear quantized due to the use of a short powerspectrum window to increase temporal resolution.

5.1.1 Bead colour

Crimson beads, (absorption/emission 625/645 nm) were compared to the yellow/green beads (505/515). These were excited with a 633 nm HeNe rather than an argon ion laser and were observed at a similar bead brightness ($\sim$ 5000 counts). Bead brightness is the important factor since that is what ultimately affects our position accuracy[1].

Figure 5.2 compares photodamage between yellow/green and crimson beads. The median speed from 0.5 s of data was calculated for 7 s and normalised to the initial speed of the bead. Initial speeds varied between $\sim$ 200 and $\sim$ 600 Hz. 8 cells were averaged for yellow/green beads and 7 averaged for crimson. Datapoints were fit with an exponential decay plus baseline to give an indication of the rate of damage. Coefficients are shown in Table 5.1. Photodamage is clearly reduced using crimson beads although damage is still quick enough to present a problem in extended measurements.

[1]Brightness is affected by laser power, the beads themselves, the filter set used and the response of the camera. This experiment was designed to produce a practical improvement rather than a quantification versus excitation or emission. Photo bleaching for beads was on a much longer timescale than photodamage and was not a factor.

Bead Colour	Brightness (counts)	Decay time (s)	Baseline
Crimson	5000	2.1	0.38
Yellow	5000	1.9	0.09
Crimson	16352	1	0.15
Crimson + his	5000	24	
Crimson + trp	5000	44	

Table 5.1: Exponential fits with baseline for photodamage experiments. Longer time constants with crimson beads at low brightness or with photo-protectants show reduced photo-damage in these cases. Baselines were not fit for histidine and tryptophan experiments as they did not slow to a flat region.

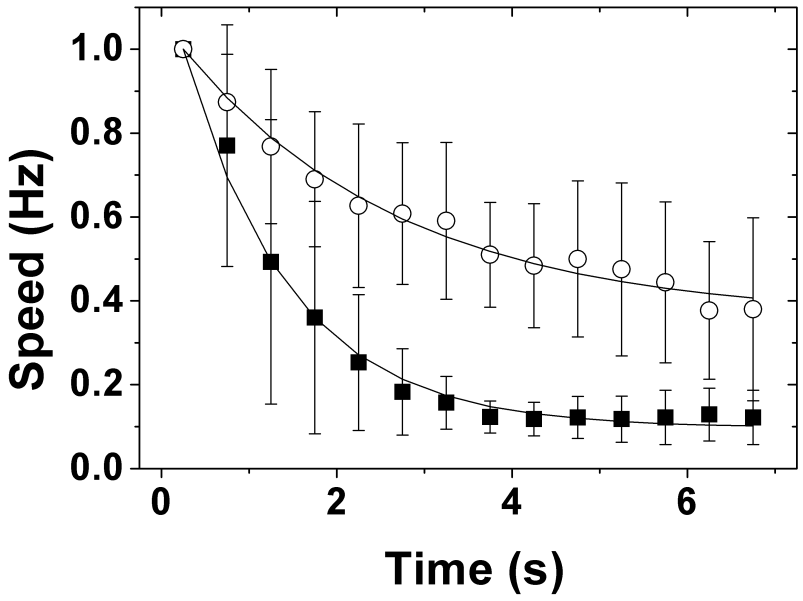

Figure 5.2: Comparison of crimson beads to yellow/green beads observed at similar brightness. The median speed from 0.5 bins was calculated and normalised to initial speed. Plotted are mean ± standard deviation for 8 and 7 measurements of yellow/green (filled squares) and crimson (open circles) beads respectively.

5.1.2 Laser power

Positional accuracy in bead location

Previous experiments were performed with beads obviously visible (on screen), at about half maximum saturation of the EMCCD camera pixels. Our analysis methods are in fact fairly robust and position localisation remains accurate at lower intensities.

The ability to localise a spot depends on both the spot size and the brightness. Spot size is a convolution of the object and the point spread function of the microscope and the contrast depends on both the number of photons from the object and the amount of background noise. The spot size in a typical experiment was about 3 pixels (standard deviation $\sim$ 130 nm) and this value was used for simulation and theoretical calculations. We also consider the pixilation introduced by our detector. With all these factors, the uncertainty in each of two dimensions is (Thompson et al., 2002),

$$\langle(\Delta x)^2\rangle = \frac{s^2 + a^2/12}{N} + \frac{8\pi s^4 b^2}{a^2 N^2},$$

where s is the spot size, a the pixel size, N the number of photons and b the standard deviation of the background. The counts per photon of our electron multiplying (EM) camera at maximum EM gain, as used in the ex-

periments, was 610 ± 70 counts per photon for the crimson beads which must be factored into our calculation when considering the number of photons[2]. Background noise, either present in the sample or introduced by the camera was effectively constant in all measurements at an intensity of about 1300 (equivalent to ~ 2 photons per pixel at 2.4 kHz). Considering the terms separately, the sampling noise ($\frac{s^2}{N}$) was larger than the pixellation noise ($\frac{a^2}{12N}$) with the background noise negligible.

Figure 5.3 shows how the ability to locate a Gaussian spot varies with brightness for our apparatus. Simulations, sampling from a 2D Gaussian spot, follow a trend similar to the theoretical accuracy as calculated from the above equation. Theory and simulation both show that the maximum positional accuracy possible for these experiments is about 5 nm or 2^o in a typical rotating bead trace. The main limitation to accuracy is the low number of photons collected at high frame rates with dim beads. The error in position for five static beads shows that in practice the position of a bead can be located to within about 7 nm or 3^o even when the bead is fairly dim.

The simulations fall close to the theoretical maximum accuracy showing our localisation algorithm was sufficiently accurate for these experiments.

[2]The manufacturer quotes pixel saturation (16352) at 200000 photons with EM gain off, corresponding to about 12 photons per count. The counts at various bead brightness and maximum EM gain, which can vary over the lifetime of the camera, were compared to EM gain off to give the calculated counts per photon.

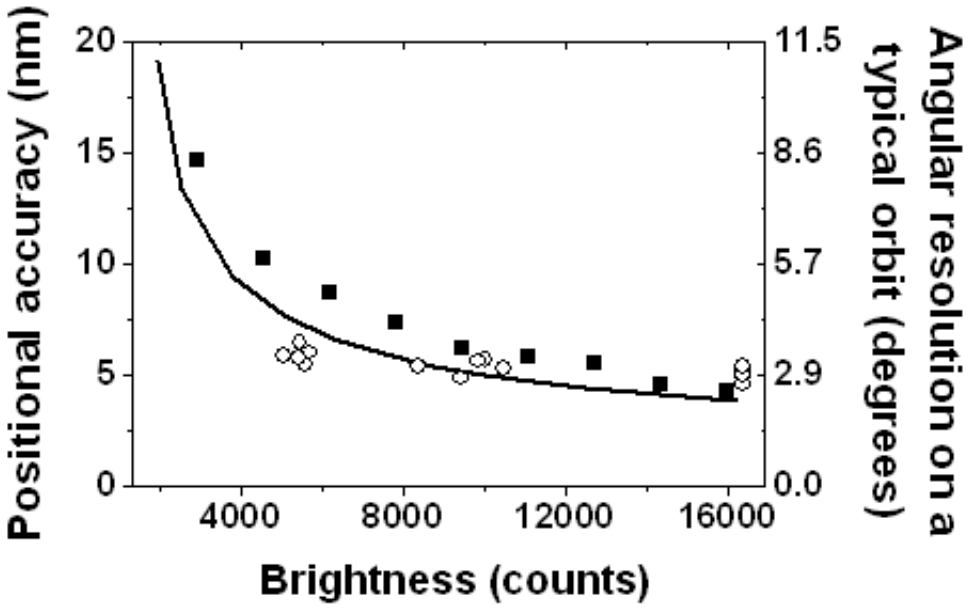

Figure 5.3: Accuracy of locating bead position. The error in position location for five beads at bright, intermediate and low illumination is shown (open circles). This is compared to simulated data (filled squares) and the theoretical maximum accuracy (solid line) under these conditions.

Photodamage

We have shown that we can accurately locate the position of a bead even at low fluorescent illumination intensity. Figure 5.4 compares the photodamage rate for spinning beads at bright (approaching saturation at 16352 counts) and dim (about 5000) pixel intensities. As for the bead colour experiments, the median speed from 0.5 s bins was calculated, normalised and averaged. The figure shows clearly that photodamage is less at lower intensities. 6 cells were averaged for bright beads with initial speeds from $\sim$ 50 to $\sim$ 400 Hz and final speeds $\sim$ 0 to $\sim$ 80 Hz. 7 cells were averaged for dim beads with initial speeds from $\sim$ 200 to $\sim$ 600 Hz and final speeds $\sim$ 30 to $\sim$ 400 Hz.

5.1.3 Reactive oxygen species

Reactive oxygen species (ROS) are suspected to be responsible for fluorescence photodamage to the motors. Histidine and tryptophan have been suggested as targets for ROS (Beghetto et al., 2000). Addition of histidine or tryptophan to the solution before fluorescent observation may suppress damage to the motor by neutralising the ROS released by the bead. Photodamage was measured with crimson beads at a brightness of $\sim$ 5000 counts.

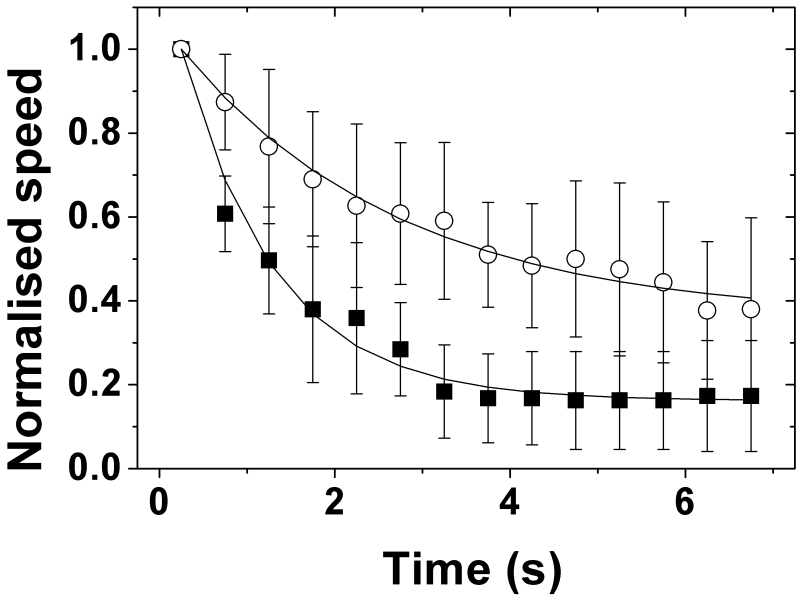

Figure 5.4: Comparison of bright beads to dim beads. The median speed from 0.5 bins was calculated and normalised to initial speed. Plotted are mean ± standard deviation for 6 and 7 measurements of bright (filled squares) and dim (open circles) beads respectively.

Histidine

Photodegradation of histidine is mediated mainly by singlet oxygen ROS ($^1O_2$). Histidine was added to the final motility solution at 5 mM. Figure 5.5 shows how photodamage is affected by the presence of histidine. The median normalised speeds show that photodamage is reduced in the presence of histidine with cells maintaining about 80 % of their initial speed after 7 seconds. Closer examination of individual cells showed less damage in slower spinning cells.

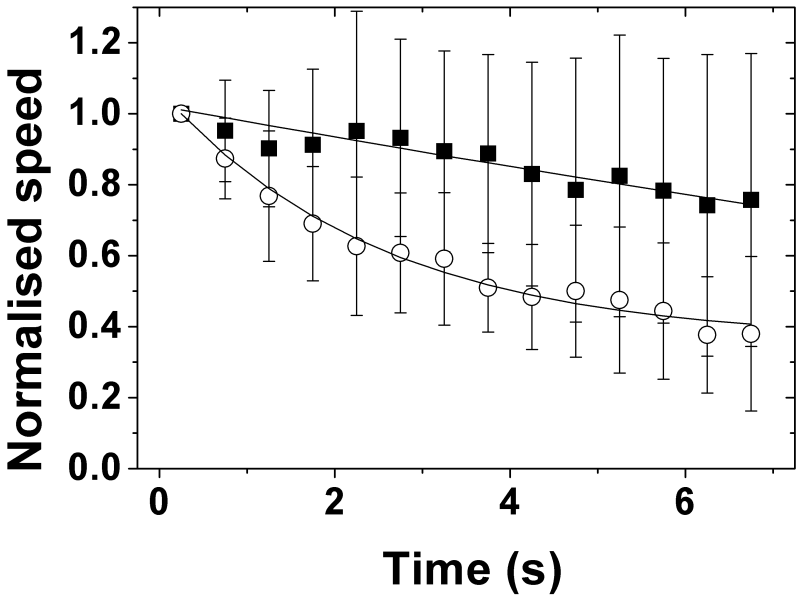

Figure 5.5: Photodamage with and without histidine present. Histidine provides some protection against fluorescent photodamage. Plotted are mean ± standard deviation for 11 and 7 measurements with (filled squares) and without (open circles) histidine respectively.

Tryptophan

Photodegradation of tryptophan is also mediated by singlet oxygen but additionally by hydroxyl radicals and hydrogen peroxide. Tryptophan should offer more protection than histidine against a wider range of photodamage mechanisms. Tryptophan was added to the final motility solution at 5 mM. Figure 5.6 shows how the photodamage is affected by the presence of tryptophan. Cells retain on average 90 % of their initial speed after 7 seconds with some cells actually increasing in speed. Closer examination of individual cells shows that like histidine, photodamage with tryptophan present was negligible for slower spinning cells. However tryptophan also provides protection for faster spinning cells.

5.1.4 Photodamage summary

Several measures have been explored to reduce photodamage to allow extended measurements of spinning motors in a non-transient state. A combination of low intensity, longer wavelength fluorescence and addition of photoprotectant species results in an assay that allows for measurements much longer than those previously performed. We have been unable to completely eliminate photodamage in faster cells but it seems that for slow spinning, perhaps single unit motors, photodamage is no longer a problem.

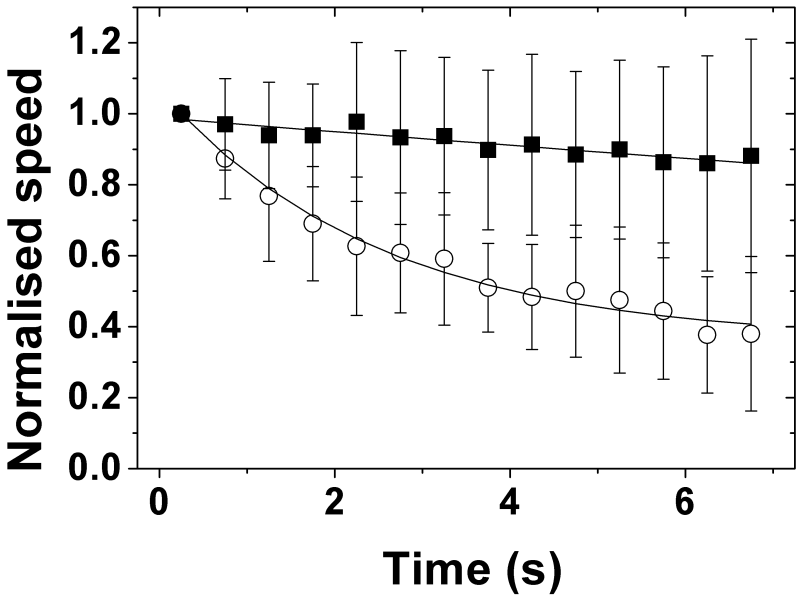

Figure 5.6: Photodamage with and without tryptophan present. Tryptophan provides good protection against fluorescent photodamage. Plotted are mean ± standard deviation for 17 and 7 measurements with (filled squares) and without (open circles) tryptophan respectively.

5.2 Sodium de-energisation

A single unit motor with a 0.5 μm bead in 85 mM sodium spins at about 35 Hz. With smaller beads the contribution of the filament stub to the drag coefficient of the rotating beads begins to dominate such that we would expect a 200 nm bead to rotate at perhaps 50 Hz under these conditions[3]. Reducing the external sodium concentration will slow down the motor but can affect the stability of rotation. The previous work used sodium de-energisation as a method of producing very slow rotation, however these motors were in a transient state. Steady rotation can be maintained by reducing sodium to about 1 mM but not much below that. This approximately halves the sodium motive force (Lo et al., 2006) producing motors that will spin at about 25 Hz.

Figure 5.7 shows how the speed of single unit motors decreases with sodium concentration in the external medium for 1 μm beads.

5.3 Steps

The previous sections detail progress towards a stable assay for the measurement of rotational steps. This work is ongoing in the lab and it is hoped that

[3]The speed of a single unit motor rotating a 200 nm bead has not been exactly measured due to the complications of photodamage.

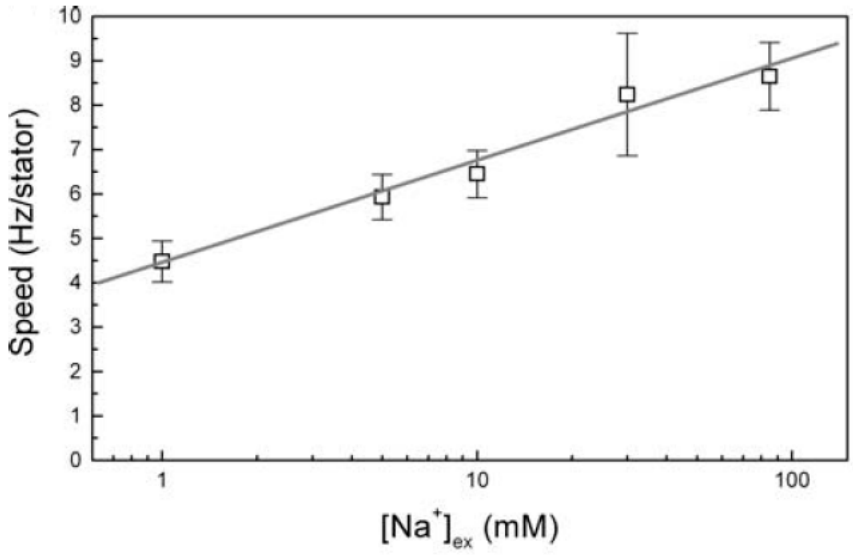

Figure 5.7: Slowing cells with sodium de-energisation. The speed per unit decreases with external sodium concentration for 1 micron beads in the Chimera strain. Stable rotation can still be observed at 1 mM external sodium where the speed is approximately half of that at 85 mM. Figure adapted from Lo et al., 2006.

in the near future these results can be used to further study the stepping of the flagellar motor.

Figure 5.8 shows an example of stepping data collected by cumulative photodamage with yellow beads. The boxed area of Figure 5.1 is examined in closer detail. Speeds are calculated per rotation with the motor angle shown below. If we expand a single rotation we observe steps consistent with those observed in the previous work of 1/26th of a revolution ($\sim 14^o$). This figure illustrates the transient nature of the rotation as observed during terminal photodamage.

The measures detailed in this chapter, both to prevent photodamage and to slow motors down maintaining stable conditions, pave the way for future studies of the motor to provide more detailed kinetic information analogous to that available for liner stepping motors such as kinesin and myosin.

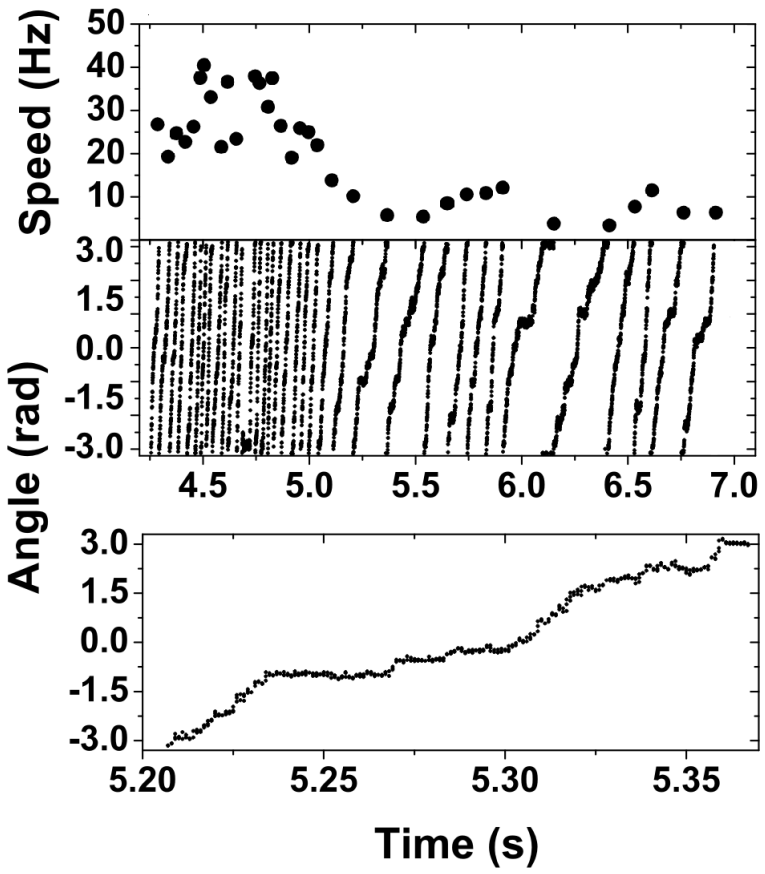

Figure 5.8: Observing rotational steps in motor rotation by cumulative photodamage. Speeds are calculated per rotation for the boxed area of Figure 5.1. Below is the angle trace for all the data followed by an expanded single rotation. Steps consistent with the previous work are observed.

Chapter 6

Conclusions

This thesis has addressed several questions relating to the topic of torque generation in the bacterial flagellar motor. The first major result to emerge is the number of torque-generating units present in a full *E. coli* motor. This result has implications for the overall energy balance of the motor as well as the assumption of independence of units. Related motor properties, the study of which is made possible by control of the number of torque generators, have also been investigated. The second major result is the development of an assay to study stable slow rotation of the motor in order to determine kinetic properties of its stepping motion. Significant progress has been made with this assay. Also arising from this thesis are several methods both ex-

perimental and analytical that can be applied to a range of problems in the future.

The number of torque-generating units in a maximally occupied flagellar motor of *E. coli* is at least eleven. In a full motor each unit present does not deliver as much torque as it would in a single unit motor. This implies an interaction between the units that were previously thought to be independent. This apparent interaction was not seen in the chimeric sodium driven units, an observation that merits further investigation. Perhaps a good starting point is the suggestion by David Blair of local proton depletion. We observe that switching is dependent on the number of torque generators although a chemotactic response to induction cannot be entirely ruled out. These results highlight two obvious areas for future research. Comparison of single, double, possibly triple unit torque-speed curves to those of full motors may provide insight into the unit interaction. Comparison to the chimeric motor is also a priority. These goals can be achieved in the near future by electrorotation methods in this laboratory. A more thorough investigation of the dependence of switching in single, double, triple unit and full motors is also underway.

This work observed discrete peaks in low induction speed histograms across a population of cells, allowing the reliable classification into single, double and triple torque-generating unit motors. This work also highlighted

the brief detachment of one or two units from the motor which is now linked to exchange of units between the motor and a membrane bound population (Leake et al., 2006).

Several methods to reduce fluorescent photodamage to motors were explored and a combination of longer wavelength, lower intensity and protective species was found to minimise this effect. During these experiments the observation of steps in the rotation of the motor, a cutting-edge result only last year, has now become routine. The materials and methods to further investigate this phenomenon have been put in place and this is an obvious avenue of future research. The position of a 200 nm fluorescent bead can be measured to within 7 nm, an impressive feat at frame rates of up to 5 kHz. The speed of analysis has been significantly improved from about an hour for a couple of seconds of data to less than a minute. Real time analysis would be a major simplification to the experimental methods and an on-line summary analysis, based on methods developed here should be incorporated into the detection software in the future.

We are a long way from a complete understanding of the flagellar motor but with each experimental result we take one more step towards this goal and learn a bit more about the most powerful and complicated of the molecular motors.

Bibliography

Adler, J. (1973), A method for measuring chemotaxis and use of the method to determine optimum conditions for chemotaxis by Escherichia coli., *J Gen Microbiol* **74**(1), 77–91.

Armstrong, J. B. and Adler, J. (1969), Location of genes for motility and chemotaxis on the Escherichia coli genetic map., *J Bacteriol* **97**(1), 156–61.

Beatson, S. A., Minamino, T. and Pallen, M. J. (2006), Variation in bacterial flagellins: from sequence to structure., *Trends Microbiol* **14**(4), 151–5.

Beghetto, C., Renken, C., Eriksson, O., Jori, G., Bernardi, P. and Ricchelli, F. (2000), Implications of the generation of reactive oxygen species by photoactivated calcein for mitochondrial studies., *Eur J Biochem* **267**(17), 5585–92.

Berg, H. C. (2003), The rotary motor of bacterial flagella., *Annu Rev Biochem* **72**, 19–54.

Berg, H. C. (2005), Swarming motility: it better be wet., *Curr Biol* **15**(15), R599–600.

Berg, H. C. and Turner, L. (1993), Torque generated by the flagellar motor of Escherichia coli., *Biophys J* **65**(5), 2201–16.

Berman, H. M., Westbrook, J., Feng, Z., Gilliland, G., Bhat, T. N., Weissig, H., Shindyalov, I. N. and Bourne, P. E. (2000), The Protein Data Bank, *Nucleic Acids Res* (28), 235–42.

Berry, R. M. (2000), Theories of rotary motors., *Philos Trans R Soc Lond B Biol Sci* **355**(1396), 503–9.

Berry, R. M. (2003), The Bacterial Flagellar Motor, *in* M. Schliwa, ed., 'Molecular Motors', Wiley-VCH, Weinheim, Germany, pp. 111–40.

Berry, R. M. and Berg, H. C. (1999), Torque generated by the flagellar motor of Escherichia coli while driven backward., *Biophys J* **76**(1 Pt 1), 580–7.

Berry, R. M., Turner, L. and Berg, H. C. (1995), Mechanical limits of bacterial flagellar motors probed by electrorotation., *Biophys J* **69**(1), 280–6.

Blair, D. F. (2003), Flagellar movement driven by proton translocation., *FEBS Lett* **545**(1), 86–95.

Blair, D. F. and Berg, H. C. (1988), Restoration of torque in defective flagellar motors., *Science* **242**(4886), 1678–81.

Block, S. M. and Berg, H. C. (1984), Successive incorporation of force-generating units in the bacterial rotary motor., *Nature* **309**(5967), 470–2.

Block, S. M., Blair, D. F. and Berg, H. C. (1989), Compliance of bacterial flagella measured with optical tweezers., *Nature* **338**(6215), 514–8.

Braun, T. F., Al-Mawsawi, L. Q., Kojima, S. and Blair, D. F. (2004), Arrangement of core membrane segments in the MotA/MotB proton-channel complex of Escherichia coli., *Biochemistry* **43**(1), 35–45.

Braun, T. F. and Blair, D. F. (2001), Targeted disulfide cross-linking of the MotB protein of Escherichia coli: evidence for two H(+) channels in the stator Complex., *Biochemistry* **40**(43), 13051–9.

Carter, N. J. and Cross, R. A. (2005), Mechanics of the kinesin step., *Nature* **435**(7040), 308–12.

Chen, X. and Berg, H. C. (2000), Torque-speed relationship of the flagellar rotary motor of Escherichia coli., *Biophys J* **78**(2), 1036–41.

Chung, S. H. and Kennedy, R. A. (1991), Forward-backward non-linear filtering technique for extracting small biological signals from noise., *J Neurosci Methods* **40**(1), 71–86.

Diez, M., Zimmermann, B., Borsch, M., Konig, M., Schweinberger, E., Steigmiller, S., Reuter, R., Felekyan, S., Kudryavtsev, V., Seidel, C. A. and Graber, P. (2004), Proton-powered subunit rotation in single membrane-bound F0F1-ATP synthase., *Nat Struct Mol Biol* **11**(2), 135–41.

Duke, T. A., Le Novere, N. and Bray, D. (2001), Conformational spread in a ring of proteins: a stochastic approach to allostery., *J Mol Biol* **308**(3), 541–53.

Engebrecht, J., Nealson, K. and Silverman, M. (1983), Bacterial bioluminescence: isolation and genetic analysis of functions from Vibrio fischeri., *Cell* **32**(3), 773–81.

Engelmann, T. (1881), Neue Methode zur Untersuchung der Sauerstoffausscheidung pflanzlicher und tierischer Organismen, *Pflugers Arch. Gesammte Physiol.* **25**, 285–92.

Engelmann, T. W. (1883), Bacterium photometricum: ein beitrag zur vergleichenden physiologie des licht und fabensinnes., *Pfluegers Arch. Gesamte Physiol.* pp. 183–86.

Fahrner, K. A., Ryu, W. S. and Berg, H. C. (2003), Biomechanics: bacterial flagellar switching under load., *Nature* **423**(6943), 938.

Finer, J. T., Mehta, A. D. and Spudich, J. A. (1995), Characterization of single actin-myosin interactions., *Biophys J* **68**(4 Suppl), 291S–296S.

Fung, D. C. and Berg, H. C. (1995), Powering the flagellar motor of Escherichia coli with an external voltage source., *Nature* **375**(6534), 809–12.

Gabel, C. V. and Berg, H. C. (2003), The speed of the flagellar rotary motor of Escherichia coli varies linearly with protonmotive force., *Proc Natl Acad Sci U S A* **100**(15), 8748–51.

Geeves, M. A. and Holmes, K. C. (1999), Structural mechanism of muscle contraction., *Annu Rev Biochem* **68**, 687–728.

Gittes, F. and Schmidt, C. (1998), Interference model for back-focal-plane displacement detection in optical tweezers, *Optics Letters* **23**(1), 7–9.

Harshey, R. M. (2003), Bacterial motility on a surface: many ways to a common goal., *Annu Rev Microbiol* **57**, 249–73.

Henrichsen, J. (1972), Bacterial surface translocation: a survey and a classification., *Bacteriol Rev* **36**(4), 478–503.

Howard, J. (1996), The movement of kinesin along microtubules., *Annu Rev Physiol* **58**, 703–29.

Hughes, K. T., Gillen, K. L., Semon, M. J. and Karlinsey, J. E. (1993), Sensing structural intermediates in bacterial flagellar assembly by export of a negative regulator., *Science* **262**(5137), 1277–80.

Itoh, H., Takahashi, A., Adachi, K., Noji, H., Yasuda, R., Yoshida, M. and Kinosita, K. (2004), Mechanically driven ATP synthesis by F1-ATPase., *Nature* **427**(6973), 465–8.

Kalir, S. and Alon, U. (2004), Using a quantitative blueprint to reprogram the dynamics of the flagella gene network., *Cell* **117**(6), 713–20.

Kalir, S., McClure, J., Pabbaraju, K., Southward, C., Ronen, M., Leibler, S., Surette, M. G. and Alon, U. (2001), Ordering genes in a flagella pathway by analysis of expression kinetics from living bacteria., *Science* **292**(5524), 2080–3.

Keener, J. P. (2005), A model for length control of flagellar hooks of Salmonella typhimurium., *J Theor Biol* **234**(2), 263–75.

Kerssemakers, J. W., Munteanu, E. L., Laan, L., Noetzel, T. L., Janson, M. E. and Dogterom, M. (2006), Assembly dynamics of microtubules at molecular resolution., *Nature* **442**(7103), 709–12.

Khan, S., Dapice, M. and Reese, T. S. (1988), Effects of mot gene expression on the structure of the flagellar motor., *J Mol Biol* **202**(3), 575–84.

Kinosita, K. . J. r., Yasuda, R., Noji, H., Ishiwata, S. and Yoshida, M. (1998), F1-ATPase: a rotary motor made of a single molecule., *Cell* **93**(1), 21–4.

Kojima, S. and Blair, D. F. (2001), Conformational change in the stator of the bacterial flagellar motor., *Biochemistry* **40**(43), 13041–50.

Kojima, S. and Blair, D. F. (2004), Solubilization and purification of the MotA/MotB complex of Escherichia coli., *Biochemistry* **43**(1), 26–34.

Korobkova, E. A., Emonet, T., Park, H. and Cluzel, P. (2006), Hidden stochastic nature of a single bacterial motor., *Phys Rev Lett* **96**(5), 058105.

Kuwajima, G. (1988), Construction of a minimum-size functional flagellin of Escherichia coli., *J Bacteriol* **170**(7), 3305–9.

Leake, M. C., Chandler, J. H., Wadhams, G. H., Bai, F., Berry, R. M. and Armitage, J. P. (2006), Stoichiometry and turnover in single, functioning membrane protein complexes., *Nature* **443**(7109), 355–8.

Leake, M. C., Wilson, D., Gautel, M. and Simmons, R. M. (2004), The elasticity of single titin molecules using a two-bead optical tweezers assay., *Biophys J* **87**(2), 1112–35.

Liang, W., Warrick, H. M. and Spudich, J. A. (1999), A structural model for phosphorylation control of Dictyostelium myosin II thick filament assembly., *J Cell Biol* **147**(5), 1039–48.

Lister, I., Schmitz, S., Walker, M., Trinick, J., Buss, F., Veigel, C. and Kendrick-Jones, J. (2004), A monomeric myosin VI with a large working stroke., *EMBO J* **23**(8), 1729–38.

Lo, C. J., Leake, M. C. and Berry, R. M. (2006), Fluorescence measurement of intracellular sodium concentration in single Escherichia coli cells., *Biophys J* **90**(1), 357–65.

Lowder, B. J., Duyvesteyn, M. D. and Blair, D. F. (2005), FliG subunit arrangement in the flagellar rotor probed by targeted cross-linking., *J Bacteriol* **187**(16), 5640–7.

Macnab, R. M. (2003), How bacteria assemble flagella., *Annu Rev Microbiol* **57**, 77–100.

Magariyama, Y., Sugiyama, S., Muramoto, K., Kawagishi, I., Imae, Y. and Kudo, S. (1995), Simultaneous measurement of bacterial flagellar rotation rate and swimming speed., *Biophys J* **69**(5), 2154–62.

Maki-Yonekura, S., Yonekura, K. and Namba, K. (2003), Domain movements of HAP2 in the cap-filament complex formation and growth process of the bacterial flagellum., *Proc Natl Acad Sci U S A* **100**(26), 15528–33.

Meister, M., Lowe, G. and Berg, H. C. (1987), The proton flux through the bacterial flagellar motor., *Cell* **49**(5), 643–50.

Minamino, T., Imae, Y., Oosawa, F., Kobayashi, Y. and Oosawa, K. (2003), Effect of intracellular pH on rotational speed of bacterial flagellar motors., *J Bacteriol* **185**(4), 1190–4.

Molloy, J. E., Burns, J. E., Kendrick-Jones, J., Tregear, R. T. and White, D. C. (1995), Movement and force produced by a single myosin head., *Nature* **378**(6553), 209–12.

Murphy, G. E., Leadbetter, J. R. and Jensen, G. J. (2006), In situ structure of the complete Treponema primitia flagellar motor., *Nature* **442**(7106), 1062–4.

Oster, G. and Wang, H. (2003*a*), How protein motors convert chemical energy into mechanical work, *in* M. Schliwa, ed., 'Molecular Motors', Wiley-VCH, Weinheim, Germany, pp. 207–27.

Oster, G. and Wang, H. (2003*b*), Rotary protein motors., *Trends Cell Biol* **13**(3), 114–21.

Oxford University Press, ed. (2002), *Oxford English Dictionary*, online edition (www.dictionary.oed.com) edn, Oxford University Press.

Paul, K. and Blair, D. F. (2006), Organization of FliN subunits in the flagellar motor of Escherichia coli., *J Bacteriol* **188**(7), 2502–11.

Pfeffer, W. (1883), Locomotorische richtungsbewegungen durch chemische rieze., *Ber. Dtsch Bot. Ges.* **1**, 524–33.

Pitta, T. P. and Berg, H. C. (1995), Self-electrophoresis is not the mechanism for motility in swimming cyanobacteria., *J Bacteriol* **177**(19), 5701–3.

Pruss, B. M. and Matsumura, P. (1997), Cell cycle regulation of flagellar genes., *J Bacteriol* **179**(17), 5602–4.

Reck-Peterson, S. L., Yildiz, A., Carter, A. P., Gennerich, A., Zhang, N. and Vale, R. D. (2006), Single-molecule analysis of dynein processivity and stepping behavior., *Cell* **126**(2), 335–48.

Reid, S. W., Leake, M. C., Chandler, J. H., Lo, C.-J., Armitage, J. P. and Berry, R. M. (2006), The maximum number of torque-generating units in the flagellar motor of Escherichia coli is at least 11, *PNAS* **103**(21), 8066–71.

Rosenfeld, S. S., Fordyce, P. M., Jefferson, G. M., King, P. H. and Block, S. M. (2003), Stepping and stretching. How kinesin uses internal strain to walk processively., *J Biol Chem* **278**(20), 18550–6.

Rowe, A. D., Leake, M. C., Morgan, H. and Berry, R. M. (2003), Rapid rotation of micron and submicron dielectric particles measured using optical tweezers, *J Mod Opt* **50**(10), 1539–54.

Ruegg, C., Veigel, C., Molloy, J. E., Schmitz, S., Sparrow, J. C. and Fink, R. H. (2002), Molecular motors: force and movement generated by single myosin II molecules., *News Physiol Sci* **17**, 213–8.

Ryu, W. S., Berry, R. M. and Berg, H. C. (2000), Torque-generating units of the flagellar motor of Escherichia coli have a high duty ratio., *Nature* **403**(6768), 444–7.

Saijo-Hamano, Y., Uchida, N., Namba, K. and Oosawa, K. (2004), In vitro characterization of FlgB, FlgC, FlgF, FlgG, and FliE, flagellar basal body proteins of Salmonella., *J Mol Biol* **339**(2), 423–35.

Samatey, F. A., Matsunami, H., Imada, K., Nagashima, S., Shaikh, T. R., Thomas, D. R., Chen, J. Z., Derosier, D. J., Kitao, A. and Namba, K. (2004), Structure of the bacterial flagellar hook and implication for the molecular universal joint mechanism., *Nature* **431**(7012), 1062–8.

Samuel, A. D. and Berg, H. C. (1995), Fluctuation analysis of rotational speeds of the bacterial flagellar motor., *Proc Natl Acad Sci U S A* **92**(8), 3502–6.

Sato, K. and Homma, M. (2000), Functional reconstitution of the Na(+)-driven polar flagellar motor component of Vibrio alginolyticus., *J Biol Chem* **275**(8), 5718–22.

Scharf, B. E., Fahrner, K. A., Turner, L. and Berg, H. C. (1998), Control of direction of flagellar rotation in bacterial chemotaxis., *Proc Natl Acad Sci U S A* **95**(1), 201–6.

Schmitt, R. (2003), Helix rotation model of the flagellar rotary motor., *Biophys J* **85**(2), 843–52.

Seeman, N. C. (2005), From genes to machines: DNA nanomechanical devices., *Trends Biochem Sci* **30**(3), 119–25.

Sellers, J. R. and Veigel, C. (2006), Walking with myosin V., *Curr Opin Cell Biol* **18**(1), 68–73.

Shaikh, T. R., Thomas, D. R., Chen, J. Z., Samatey, F. A., Matsunami, H., Imada, K., Namba, K. and Derosier, D. J. (2005), A partial atomic structure for the flagellar hook of Salmonella typhimurium., *Proc Natl Acad Sci U S A* **102**(4), 1023–8.

Shao, Q. and Gao, Y. Q. (2006), On the hand-over-hand mechanism of kinesin., *Proc Natl Acad Sci U S A* **103**(21), 8072–7.

Shimabukuro, K., Yasuda, R., Muneyuki, E., Hara, K. Y., Kinosita, K. . J. r. and Yoshida, M. (2003), Catalysis and rotation of F1 motor: cleavage

of ATP at the catalytic site occurs in 1 ms before 40 degree substep rotation., *Proc Natl Acad Sci U S A* **100**(25), 14731–6.

Silverman, M. and Simon, M. (1974), Flagellar rotation and the mechanism of bacterial motility., *Nature* **249**(452), 73–4.

Skerker, J. M. and Berg, H. C. (2001), Direct observation of extension and retraction of type IV pili., *Proc Natl Acad Sci U S A* **98**(12), 6901–4.

Sowa, Y., Hotta, H., Homma, M. and Ishijima, A. (2003), Torque-speed relationship of the Na+-driven flagellar motor of Vibrio alginolyticus., *J Mol Biol* **327**(5), 1043–51.

Sowa, Y., Rowe, A. D., Leake, M. C., Yakushi, T., Homma, M., Ishijima, A. and Berry, R. M. (2005), Direct observation of steps in rotation of the bacterial flagellar motor., *Nature* **437**(7060), 916–9.

Suzuki, H., Yonekura, K. and Namba, K. (2004), Structure of the rotor of the bacterial flagellar motor revealed by electron cryomicroscopy and single-particle image analysis., *J Mol Biol* **337**(1), 105–13.

Takagi, Y., Homsher, E. E., Goldman, Y. E. and Shuman, H. (2006), Force generation in single conventional actomyosin complexes under high dynamic load., *Biophys J* **90**(4), 1295–307.

Thompson, R. E., Larson, D. R. and Webb, W. W. (2002), Precise nanometer localization analysis for individual fluorescent probes., *Biophys J* **82**(5), 2775–83.

Veigel, C., Coluccio, L. M., Jontes, J. D., Sparrow, J. C., Milligan, R. A. and Molloy, J. E. (1999), The motor protein myosin-I produces its working stroke in two steps., *Nature* **398**(6727), 530–3.

Wadhams, G. H. and Armitage, J. P. (2004), Making sense of it all: bacterial chemotaxis., *Nat Rev Mol Cell Biol* **5**(12), 1024–37.

Weber, J. and Senior, A. E. (2003), ATP synthesis driven by proton transport in F1F0-ATP synthase., *FEBS Lett* **545**(1), 61–70.

Wikipedia contributors (2006), Life, *in* 'http://en.wikipedia.org/wiki/Life', Wikipedia, The Free Encyclopedia.

Xing, J., Bai, F., Berry, R. and Oster, G. (2006), Torque-speed relationship of the bacterial flagellar motor., *Proc Natl Acad Sci U S A* **103**(5), 1260–5.

Yakushi, T., Yang, J., Fukuoka, H., Homma, M. and Blair, D. F. (2006), Roles of charged residues of rotor and stator in flagellar rotation: comparative study using H+-driven and Na+-driven motors in Escherichia coli., *J Bacteriol* **188**(4), 1466–72.

Yasuda, R., Noji, H., Yoshida, M., Kinosita, K. . J. r. and Itoh, H. (2001), Resolution of distinct rotational substeps by submillisecond kinetic analysis of F1-ATPase., *Nature* **410**(6831), 898–904.

Yildiz, A., Tomishige, M., Vale, R. D. and Selvin, P. R. (2004), Kinesin walks hand-over-hand., *Science* **303**(5658), 676–8.

Yonekura, K., Maki-Yonekura, S. and Namba, K. (2003), Complete atomic model of the bacterial flagellar filament by electron cryomicroscopy., *Nature* **424**(6949), 643–50.